High Efficiency GaAs-based Solar Cells Simulation and Fabrication

by

Chaomin Zhang

A Thesis Presented in Partial Fulfillment
of the Requirements for the Degree
Master of Science

Approved April 2014 by the
Graduate Supervisory Committee:

Christiana Honsberg, Chair
Nikolai Faleev
Stephen Goodnick

ARIZONA STATE UNIVERSITY

May 2014

ABSTRACT

GaAs-based solar cells have attracted much interest because of their high conversion efficiencies of ~28% under one sun illumination. The main carrier recombination mechanisms in the GaAs-based solar cells are surface recombination, radiative recombination and non-radiative recombination. Photon recycling reduces the effect of radiative recombination and is an approach to obtain the device performance described by detailed balance theory. The photon recycling model has been developed and was applied to investigate the loss mechanisms in the state-of-the-art GaAs-based solar cell structures using PC1D software.

A standard fabrication process of the GaAs-based solar cells is as follows: wafer preparation, individual cell isolation by mesa, n- and p-type metallization, rapid thermal annealing (RTA), cap layer etching, and anti-reflection coating (ARC). The growth rate for GaAs-based materials is one of critical factors to determine the cost for the growth of GaAs-based solar cells. The cost for fabricating GaAs-based solar cells can be reduced if the growth rate is increased without degrading the crystalline quality. The solar cell wafers grown at different growth rates of 14 μm/hour and 55 μm/hour were discussed in this work. The structural properties of the wafers were characterized by X-ray diffraction (XRD) to identify the crystalline quality, and then the as-grown wafers were fabricated into solar cell devices under the same process conditions. The optical and electrical properties such as surface reflection, external quantum efficiency (EQE), dark I-V, Suns-V_{oc}, and illuminated I-V under one sun using a solar simulator were measured to compare

the performances of the solar cells with different growth rates. Some simulations in PC1D have been demonstrated to investigate the reasons of the different device performances between fast growth and slow growth structures. A further analysis of the minority carrier lifetime is needed to investigate into the difference in device performances.

To my parents for their love and support

ACKNOWLEDGMENTS

First of all, I would like to thank my advisor Dr. Christiana Honsberg for her support and encouragement throughout this work. Under her continuous guidance I learnt much and I have the opportunities to expand my knowledgebase. I would like to thank Dr. Stephen Goodnick, who is always enthusiastic and patient to help me and support me. And I am grateful to Dr. Nicolai Faleev who helped me a lot including helping me analysis wafers via XRD and giving me academic guidance. I much appreciate that all of them spending their valuable time in revising my thesis.

Also, I am very grateful to have worked with Yeongho Kim, who is a great researcher and friend and who helped me a lot all the time including solar cell fabrication and thesis writing. Without his help, I don't think I can finish all the work. I would also like to give thanks to Jacob Beck who helped me in measuring the I-V curves using the solar simulator in his lab. The some conversations about photon recycling with Yuan Zhao also help me a lot.

I would also like to give lots of thanks to all friends who ever helped me either in work or in life. Especially, I would like to thank my friend Jingda Wu from University of Washington who helped me revised my thesis.

TABLE OF CONTENTS

Page

LIST OF TABLES

LIST OF FIGURES

CHAPTER 1

INTRODUCTION

Energy is the most important factor affecting the development of modern countries. The growing population and rapidly developing economies cause the booming consumption of energy. Currently, a majority of the world's electricity supply is generated from fossil fuels such as coal, oil and nature gas. However, these traditional energy sources are facing a series of issues including the decrease of fossil fuels, security concerns caused by fossil fuel supplies and the growing environmental concerns due to the burning of fossil fuels leading to more greenhouse gas emissions. One solution to these issues is the development of alternative energy sources and new technologies for electricity generation. Renewable energy sources including wind energy, solar energy, and hydroelectric generation have huge potential to take the place of fossil fuels which have finite resources.

Solar energy, which is available in most of the areas over the world, as shown in Fig. 1.1, has emerged as one of the most rapidly growing renewable energy sources. Theoretically, solar energy is free and virtually limitless which make it become an ideal energy source. The power of the sunlight that reaches the earth's surface in one year is more than 10,000 times than the world's yearly energy needs. How to harvest this large power in an efficient and inexpensive way is a goal for scientists. As shown in Fig. 1.2 which records the great effort of scientists in the world in the last 40 years, there are many kinds of research on solar technologies are attempted including thin-film, single-

junction cells, organic cells, quantum dot cells, dye-sensitized cells and also new kinds of material or technologies are emerging every year.

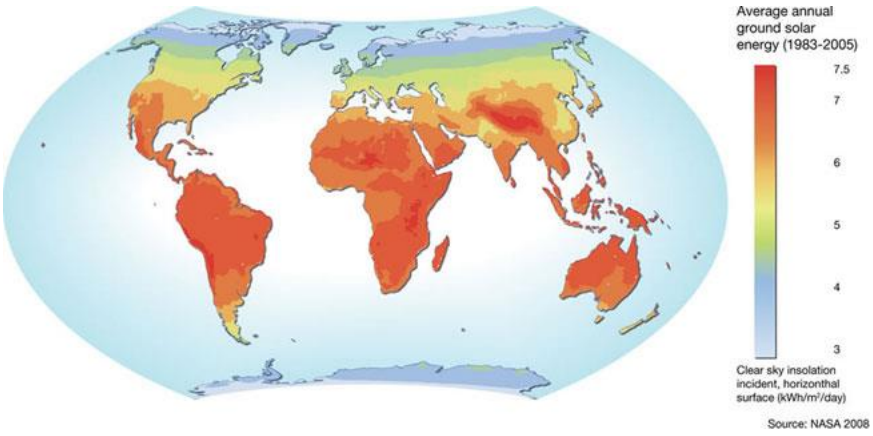

Fig. 1.1 Global solar energy distribution. *Courtesy of NASA, 2008*

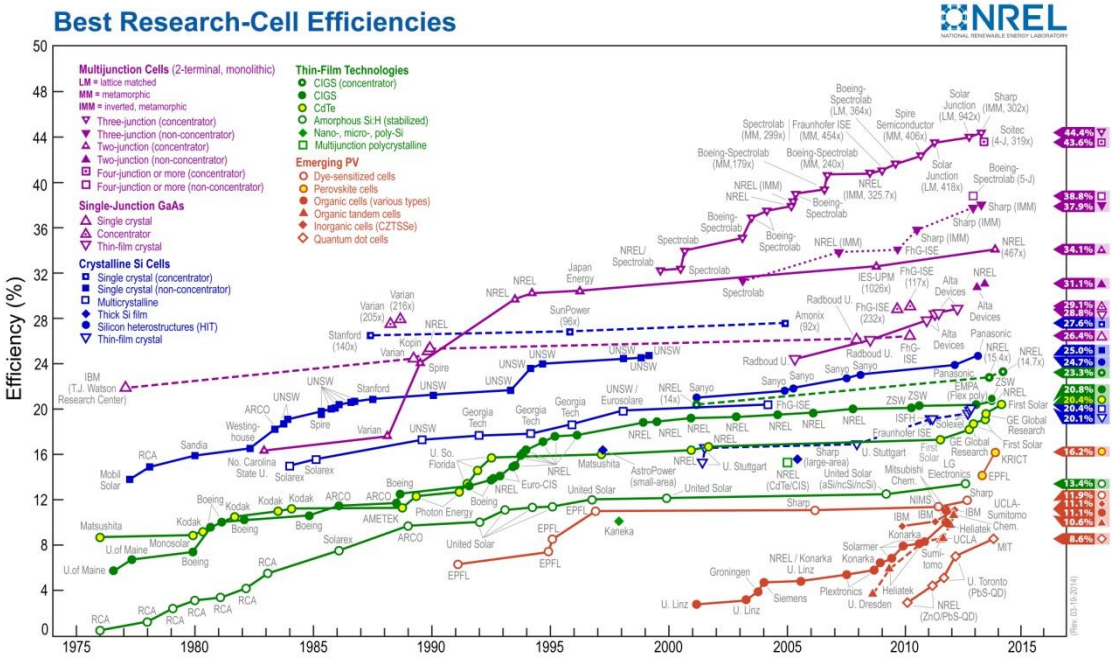

Fig. 1.2 The best research-cell efficiencies from 1975 to 2014

The development of single-junction GaAs solar cells has been fast in last 10 years, and the efficiency is up to 28.8% under one sun which is the most efficient for single junction solar cells to date according to Fig. 1.2. The efficiency of GaAs solar cells has reached 29.1% under concentrated sun light. GaAs solar cells are highly efficiency devices, however, they are too expensive for terrestrial large-area applications because of the high device fabrication cost and the availability of relatively rare elements (In, Ga) [1].

In order to make GaAs-based solar cells be widely used, the direct ways to solve this problem are to improve the efficiency and reduce the fabrication cost. Firstly, making thin solar cells is a pathway to decrease the use of material. GaAs has direct bandgap and correspondingly high absorption coefficient which is ideally suited for thin solar cells. Improving the photon recycling effect in GaAs solar cell is the key to get high performance thin solar cells. The photon recycling model will be built and the record GaAs-based solar cells will be investigated via PC1D simulation to further improve the efficiency.

Secondly, with higher growth rates, GaAs-based solar cells process time can be reduced and so the cost of the epitaxial layers used in relative structures can also be lowered. GaAs-based solar cells are usually grown by metal-organic chemical vapour deposition (MOCVD). Increasing the growth rate of GaAs is a possible way to decrease the cost for wafer fabrication. In this thesis, the fabrication method of GaAs-based solar

cells will be introduced, and the performance of the GaAs-based solar cells with different growth rates of GaAs from 14 μm/hour up to 55 μm/hour will be discussed.

In this thesis, Chapter 2 is an introduction to the operation principles of solar cells and the main recombination mechanisms in GaAs solar cells. A photon recycling model is built and the simulation of state-of-the-art GaAs cells is introduced in Chapter 3. In Chapter 4, the common fabrication processes of GaAs-based solar cells are described. The Characterizations of fast growth and slow growth GaAs-based solar cells are compared and analyzed in Chapter 5. Finally, a summary of this work is given and the future work is mentioned in Chapter 6.

CHAPTER 2

GAAS SOLAR CELLS

2.1 Physics of Solar cells

Semiconductor solar cells are based on the physics that semiconductors have the ability to absorb light and transfer a portion of the absorbed photons energy into electrical current in the form of electrons and holes. The semiconductor diode will divide and collect electrons and holes in special directions and form an electrical current.

Fig. 2.1 shows the structure of a conventional solar cell. When sunlight is incident on the surface of the cell, electrons and holes are generated. Holes are collected to rear contact and electrons are collected to finger contact. Antireflective coating reduces the surface reflection of sunlight on the solar cells.

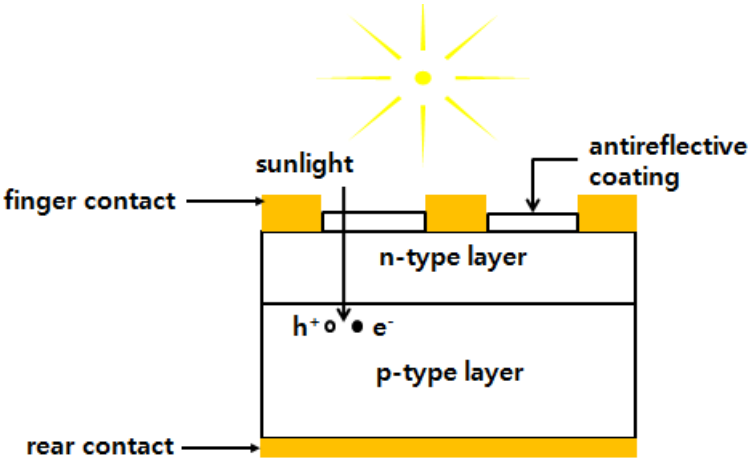

Fig. 2.1 The structure of a simple conventional solar cell

The efficiency of solar cells is sensitive to both intensity and spectrum of incident light. To predict the performance of solar cells in space, the spectral distribution of sunlight that just above the Earth's atmosphere is used and it is referred to AM0 radiation spectrum which the radiation intensity is about 1.353kW/m^2 [2]. The standard spectrum on the Earth's surface is usually referred to AM1.5G [3] which includes direct and diffuse radiation and the radiation intensity of AM1.5G standard spectrum is normalized to 1kW/m^2.

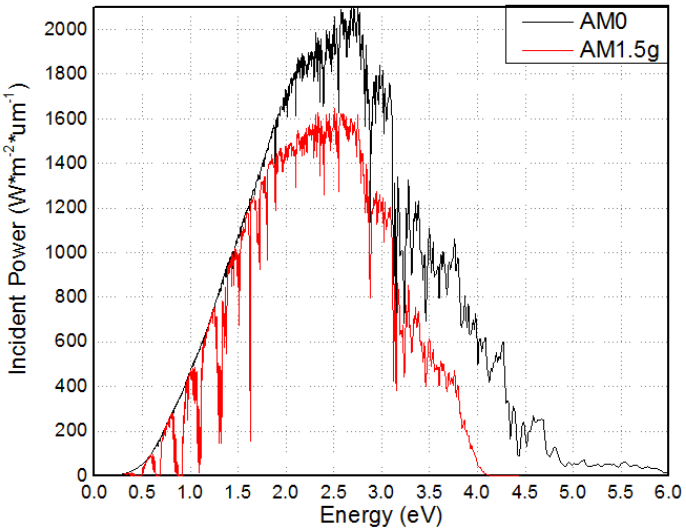

Fig. 2.2 The radiation spectrum for AM0 and AM1.5G

From Fig. 2.3, on the basis of a lumped equivalent circuit model, and application of Kirchhoff's rules, Eq. (2.1) can be obtained, where I_L is the current at load, I_s is the saturation current, R_s is the series resistant, R_{sh} is the shunt resistant.

$$ln\left(\frac{I+I_L}{I_s}-\frac{V-IR_S}{I_sR_{sh}}+1\right)=\frac{q}{kT}(V-IR_s) \tag{2.1}$$

The efficiency of solar cells can be obtained from Eq. (2.2):

$$\eta = \frac{P_{max}}{P_{in}} = \frac{I_{sc} \times V_{oc} \times FF}{P_{in}} \tag{2.2}$$

where I_{sc} is short circuit current, V_{oc} is open circuit voltage, P_{in} is the incident sunlight power and FF is the fill factor, which is given by:

$$FF = \frac{I_{MP} \times V_{MP}}{I_{sc} \times V_{oc}} \tag{2.3}$$

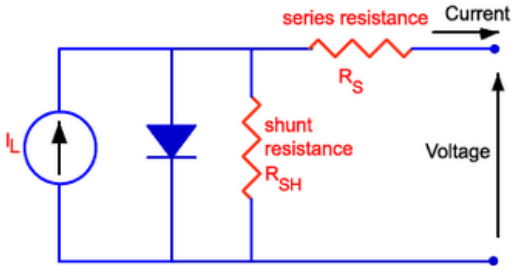

Fig. 2.3 Parasitic series and shunt resistances in a solar cell circuit

The maximum output power $P_{MP}=I_{MP} \times V_{MP}=FF \times I_{sc} \times V_{oc}$. To get higher P_{MP} or efficiency, larger I_{sc} and V_{oc} are required. Larger E_g is needed to increase V_{oc}, but causes decrease in I_{sc} due to less photons absorbed at larger E_g. Therefore, E_g needs to be an intermediate value for optimum P_{max}.

2.2 Recombination Processes

Carrier recombination can be caused by any defect or impurity within or at the surface of semiconductor. In GaAs solar cells, there are four main recombination processes, including surface recombination, radiative recombination, SRH recombination and Auger recombination as seen in Fig. 2.4.

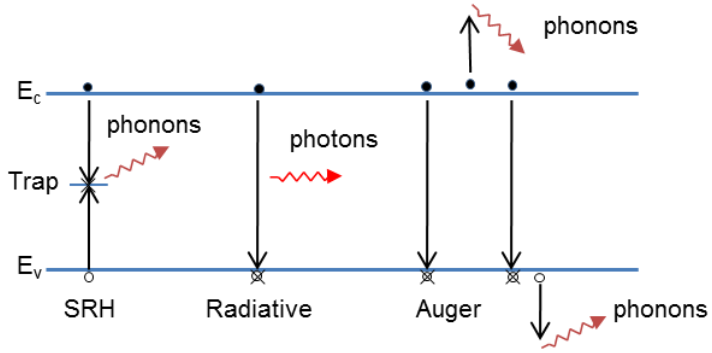

Fig. 2.4 Recombination processes in semiconductor

2.2.1 Surface recombination

The minimization of surface recombination plays a vital role in high performance solar cells, especially in the case of thin solar cells. The interruption of periodicity at the crystal surface leads to dangling bonds acting as an inherent source of deep-level defects. These surface states exist in the forbidden gap. The high recombination at the surface of solar cells depletes the minority carriers in the area of the surface which results in the carriers from surrounding that is higher concentration region flowing into the surface region by diffusion. Therefore, the surface recombination velocity S_r which is the velocity rate that minority carriers move towards the surface, in units of cm/sec, is introduced to specify the surface recombination. The higher velocity S_r, the larger surface recombination, and vice versa. In addition to defects from the break in periodicity, the impurities at the surface ranging from the dust to metals usually are a source of surface states.

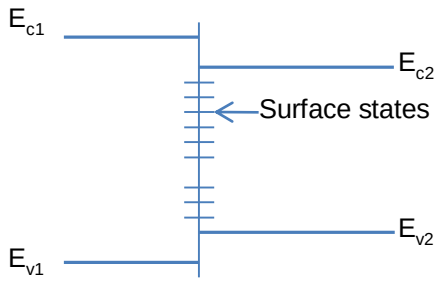

Fig. 2.5 Illustration of surface states at a semiconductor surface or interface between dissimilar materials

Experimental work [4], [5] indicates that the surface recombination velocity is high and exceeds 10^7 cm/s on the free GaAs surface. Different treatments on the GaAs surfaces and interfaces and different doping level contribute to different surface recombination velocity ranging from 10^5 to 10^7 cm/s as shown in the reference [6]-[9]. From these literatures, higher doping level in the bulk tends to have higher surface recombination.

In order to achieve low surface recombination velocity, which corresponds to a low surface recombination rate, it is necessary to reduce the number of dangling bonds, which known as surface passivation. S_r can be reduced either by growing a layer on the top of the semiconductor surface or chemical treatment as described in [10]-[12]. When another epitaxially grown material on the semiconductor surface forms a hetero-junction interface, the issue of lattice matching becomes vital due to misfit dislocations causing defects. As shown in Fig. 2.6, the lattice constant of InAs, InP, AlAs, AlP and GaP are close to that of GaAs. Two kinds of compound systems, $Al_xGa_{1-x}As$ and $In_xGa_{1-x}P$, can be lattice-matched and wider bandgap materials for GaAs. AlGaAs [13], [14] layer is widely

used for passivation layers and is often considered as a standard window material [15] and it is essential to GaAs device technology. For x≈0.5, $Ga_xIn_{1-x}P$ has the same lattice constant as GaAs with the band gap energy of 1.8-1.9eV and Olsen et al. [16] first used it as a passivating window layer in GaAs solar cell. Olson et al. [14] compared the interface surface recombination velocity for $Al_{0.4}Ga_{0.6}As$/GaAs and $In_{0.5}Ga_{0.5}P$/GaAs double heterojunction structures and concluded that AlGaAs/GaAs interface is more likely to be contaminated by oxygen related deep levels which resulting in higher surface recombination. Either AlGaAs or InGaP layers epitaxially deposited on GaAs surfaces can decrease significantly the surface recombination [17].

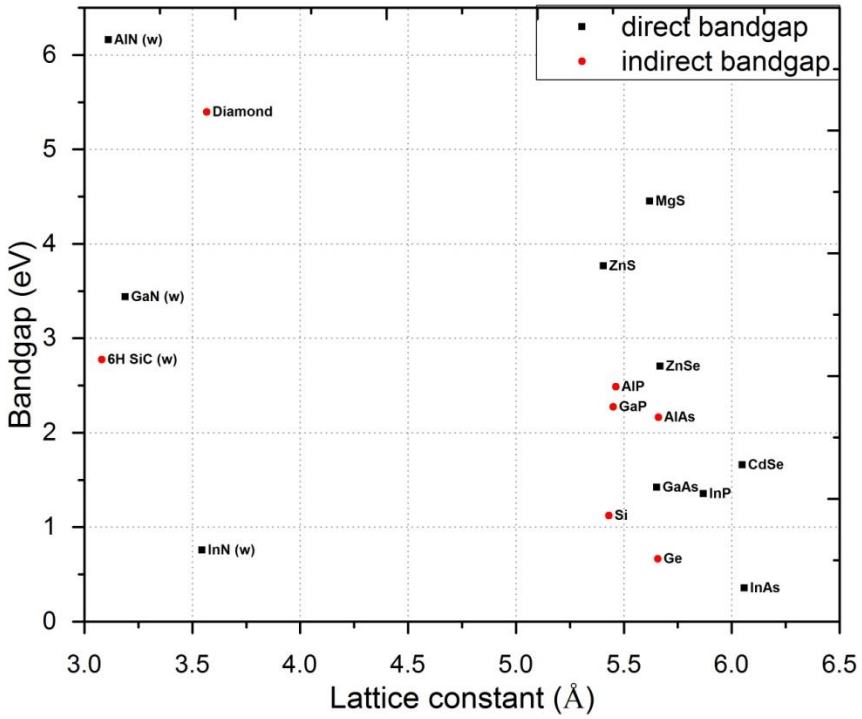

Fig. 2.6 Lattice parameters and bandgaps at 300k

2.2.2 Radiative recombination

Radiative recombination, i.e. band to band recombination, is a reverse process of light absorption in solar cells that electrons from conduction band recombine with the holes from valence band and produce photons. This effect is much more efficient in direct bandgap semiconductors, like GaAs, rather than in indirect bandgap semiconductors, like Si. The photon emission is the essential principle in semiconductor lasers and light emitting diodes (LED). In high quality GaAs solar cells, radiative recombination is dominant [18]. The net radiative recombination is given by:

$$R_{rad} = B(pn - n_i^2) \tag{2.4}$$

where B is radiative recombination coefficient, p and n are the doping level of semiconductor, and n_i is the intrinsic carrier density.

D.Z Garbuzov [19] introduced a simple quantum-mechanical calculation for direct-bandgap semiconductors and obtained the B-coefficient using the following expression:

$$B = 3 \times 10^{-10} \times \left(\frac{E_g}{1.5}\right)^2 \left(\frac{300}{T}\right)^{1.5} \tag{2.5}$$

Putting in the bandgap of GaAs at room temperature which is 1.424eV, one gets B to be about 2.7 $\times 10^{-10}$ cm^3/s comparing to a value of 1.1 x 10^{-14} cm^3/s [20] in silicon.

2.2.3 Non-radiative recombination in bulk

There are two main non-radiative recombination processes in GaAs: Shockley-Read-Hall recombination (SRH) and Auger recombination. SRH recombination [21] is

the recombination through defects which form energy states in the forbidden region and trap electrons or holes. Thus, the holes from valence band or electrons from conduction band recombine with the carriers in the trap energy level resulting in emitting phonons. The defects can be introduced during the processes, such as doping process. The bulk carrier lifetime is inversely proportional to the trap concentration that $\tau_{SRH}=1/(\sigma \times v_{th} \times N_T)$, where σ is the capture cross-section, v_{th} is the thermal velocity of the carriers and N_T is the density of traps. When there are more than one deep-level defect types in the semiconductor, the total SRH low-injection lifetime τ_{SRH} is described by:

$$\frac{1}{\tau_{SRH}} = \sum_i \frac{1}{\tau_i} \tag{2.6}$$

where, τ_i is the Shockley-Read-Hall lifetime for each specific type of defect.

Auger recombination [22] is another non-radiative recombination process that transfers the energy by electron-hole recombination translates to a third carrier where phonons are finally emitted in the semiconductor as shown in Fig. 2.4. The Auger recombination rate can be estimated by

$$R_{Auger} = \left(C_n n + C_p p\right)(pn - n_i^2) \tag{2.7}$$

where, C_n, C_p are Auger coefficients and n, p are minority carrier doping concentration. In GaAs-based solar cells, Auger recombination cannot be ignored at the situation of high doping density or high injection levels caused by high concentrated sunlight. The Auger recombination also limits the effective lifetime, thus the efficiency, of silicon-based solar cells.

2.3 GaAs solar cells

As shown in Fig. 2.7, the light absorption rate for GaAs is much higher than crystal silicon and amorphous silicon when the photon energy is close to the bandgap. Based on the fact that the sunlight can be effectively absorbed in a few micro-meters, GaAs is an excellent material candidate for thin solar cells. The conventional structure of GaAs solar cells is shown in Fig. 2.8. The window layer is a wide-bandgap material, like AlGaAs, which is used to process high-energy photons, allowing low-energy photons to pass through. Another function of window layer is to reduce surface recombination. Above the window layer, a heavily doping cap layer is usually grown to protect window layer and acts as a contact layer. The emitter layer and base layer are either n-p or p-n doped GaAs layers to form absorption layers. At the rear surface of the solar cells, a BSF, or back surface field layer which is also a wide-bandgap material is a highly doped region forming a potential barrier to minority carrier flow to the rear surface.

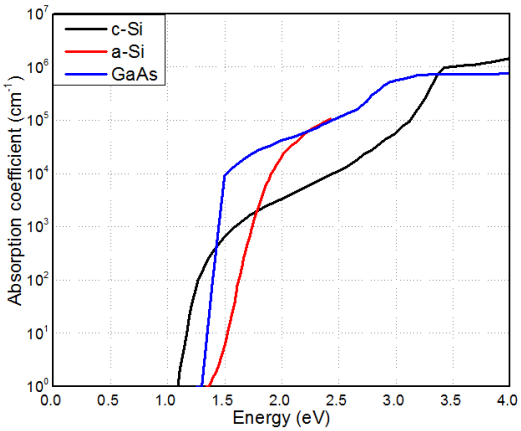

Fig. 2.7 Absorption coefficient of c-Si, a-Si and GaAs

Fig. 2.8 The conventional structure of GaAs solar cells

GaAs is a direct band gap which can be used to emit photons efficiently. Since 1962, GaAs has been used to produce laser diodes [23]. The first GaAs heterostucture solar cells were created by Zhores Alferov's group in USSR in 1970 [24]. The development of GaAs solar cells has been rapid in the last 30 years. In the early 1980s, the best GaAs solar cells were already better than Si solar cells in efficiency. From 1990 to 2007, the record efficiency of GaAs solar cells stayed constant at 25.1% [25]. G.J. Bauhuis et al. broke the record and obtained 26.1% using epitaxial lift-off (ELO) technique which separated the solar cell structure from its substrate in 2008 [26]. ELO can produce high quality GaAs solar cells [18]. The ELO process uses inverted epitaxial growth [27] and selective etching of a release layer that removes the substrate as shown in Fig. 2.9. A metal layer acting as a reflector is usually deposited on the BSF layer which can be used to improve photon recycling. ELO is realized by the high etch selectivity of $Al_xGa_{1-x}As$ alloys in hydrofluoric acid [28]. After etching the release layer, the host substrate can be reused which can reduce the manufacturing cost. With high quality GaAs solar cells, in 2010 the record reached 26.4% [29] by Fraunhofer ISE, and later, by maximizing the photon recycling effect, 28.8% was obtained in 2012 [30] by Alta Devices.

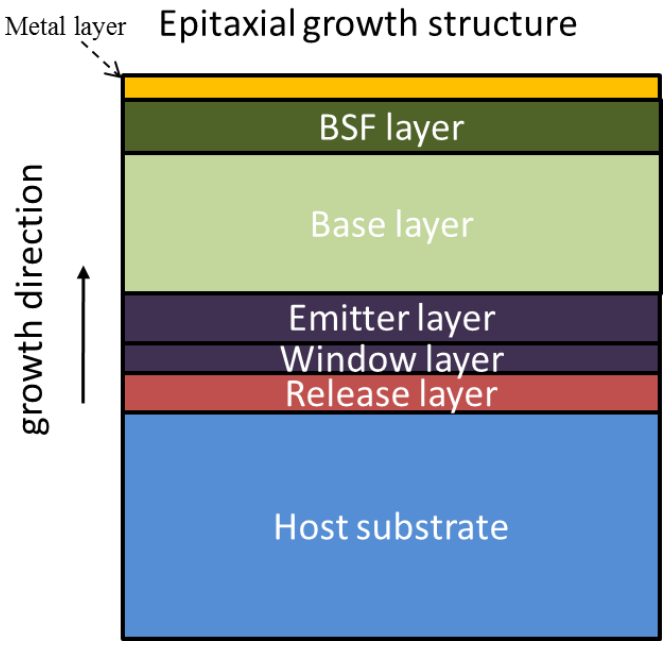

Fig. 2.9 Epitaxial growth structure using ELO technology

CHAPTER 3

DEVICE MODELING OF GAAS-BASED SOLAR CELLS

Photon recycling is a critical solution to realize high efficiency solar cells which are close to the detailed balance limit. In this chapter, a photon recycling model is developed and demonstrated by modeling the highest efficiency GaAs solar cells by Alta devices. The simulation program used is PC1D, which is software that solves the fully coupled nonlinear equations for the quasi-one-dimensional transport of electrons and holes in crystalline semiconductor devices.

3.1 Detailed balance limit

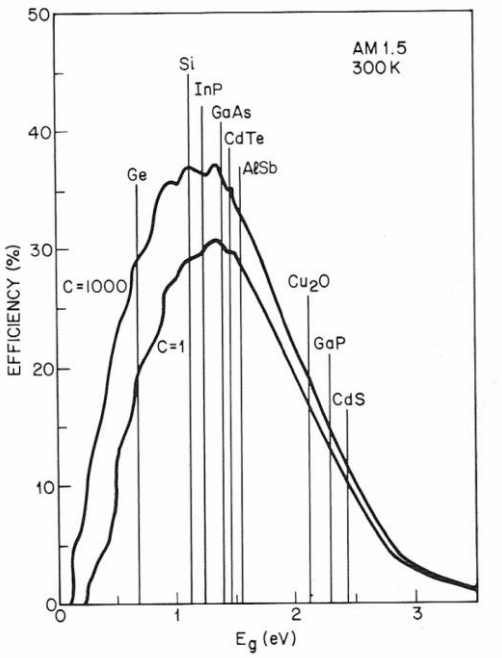

Fig. 3.1 Solar-cell efficiency versus energy bandgap under solar concentrations of 1and 1000 suns [31]

The detailed balance limit for solar cells was introduced by Shockley and Queisser in 1961 [32]. In general, only two intrinsic losses are considered in detailed balance model, one is the unabsorbed energy loss that photons whose energy is below bandgap cannot be absorbed, and the other one is radiative recombination loss. Other types of losses automatically show up, such as thermalization losses. The efficiency limit predicted by this model is called detailed balance limit. Shockley and Queisser calculated the detailed balance limit using 6000-K blackbody spectrum and calculated the intrinsic radiative flux using the detailed balance principle. C. H. Henry [31] extended their approach by using a standard air mass (AM) 1.5 terrestrial spectrum. As calculated by Henry [31], considering the E_g and radiative recombination, optimum E_g for single-junction solar cells is about 1.4eV as shown in Fig. 3.1. The maximum efficiency is 31% at a concentration of 1 sun and 37%, 50%, 56% and 72% for the cells with 1, 2, 3, and 36 energy gaps, respectively, can be achieved at 1000 suns concentration at room temperature (300K). The bandgap of GaAs is close to the optimum E_g for single junction solar cells whose maximum efficiency is above 30%. Therefore, GaAs is capable of obtaining high efficiency (>30%) according to the detailed balance model.

Nowadays, quite high-quality crystalline GaAs solar cells can be achieved that the internal luminescence yield is more than 99% [18] and the radiative recombination is the dominant recombination mechanism. Reducing the effect of radiative recombination efficiently by increasing the re-absorption effect is one feasible solution to approach the detailed balance limit.

3.2 Photon recycling in GaAs solar cells

Photon recycling describes the re-absorption and generation of new electron-hole pairs from photons arising from self-emission by radiative recombination in semiconductors. These photons from self-emission may escape out of the material or may be re-absorbed. For direct bandgap semiconductors, the absorption rate rises steeply to 1×10^4 cm^{-1} as shown in Fig. 2.7 when photon's energy is higher than the bandgap of material, as a result, the self-absorption effect is quite strong in direct semiconductors according to the van Roosbroeck-Shockley relationship [33]. The energy of the emitted photon in a radiative recombination event is high enough to be absorbed and create another electron-hole pair in direct bandgap semiconductors. This photon recycling or self-excitation phenomenon was first studied at 1957 [34]. Further study shows this effect can be reduced with high surface recombination and large carrier diffusion length [35]. Asbeck [36] made some explanations of photon recycling and proposed a parameter average lifetime enhancement Φ_{PR} to describe photon recycling with the effective radiative lifetime written as:

$$\frac{1}{\tau_R} \rightarrow \frac{1}{\phi_{PR}\tau_R} \tag{3.1}$$

The factor Φ_{PR} is different for specific device structure because its value depends on many parameters including thickness and doping concentration.

Here the structure of GaAs solar cells in Fig. 3.2 is studied to find out how the thickness of base layer of GaAs solar cells affects the device performances of the cells

and solutions to reduce radiative recombination which is demonstrated via the simulation program PC1D.

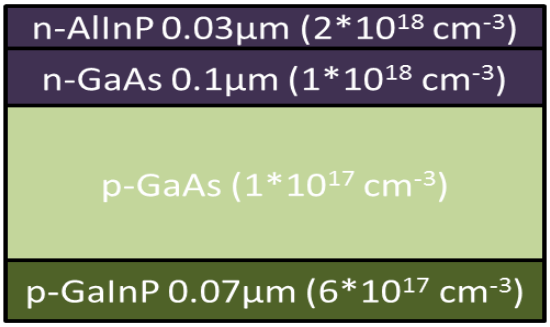

Fig. 3.2 GaAs solar cell structure for simulating the effect of Emitter thickness and photon recycling on the device performances

The thickness of p-GaAs varies from 0.25μm to 3μm. Other parameters are: SRH lifetime τ_{SRH}=1μs; assuming that the surface recombination S_r at the every surface/interface is small that can be ignored. The front reflection loss with anti-reflection coating is considered to be 1%. The light that escapes from front [37] is $1/(4n^2)\approx 2\%$. The rear reflector is 0% (GaAs substrate) or 90%. In PC1D, photon recycling is realized via decreasing the value of radiative coefficient B. The value of $B=2\times10^{-10}cm^3/s$ is used to present no photon recycling in this simulation and $B=2\times10^{-11}cm^3/s$ for the value of B including photon recycling.

Therefore the following three cases are concerned:

Case1: without rear reflector, $B=2\times10^{-10}cm^3/s$

Case2: with rear reflector (90% reflection), $B=2\times10^{-10}cm^3/s$

Case3: with rear reflector (90% reflection), $B=2\times10^{-11}cm^3/s$

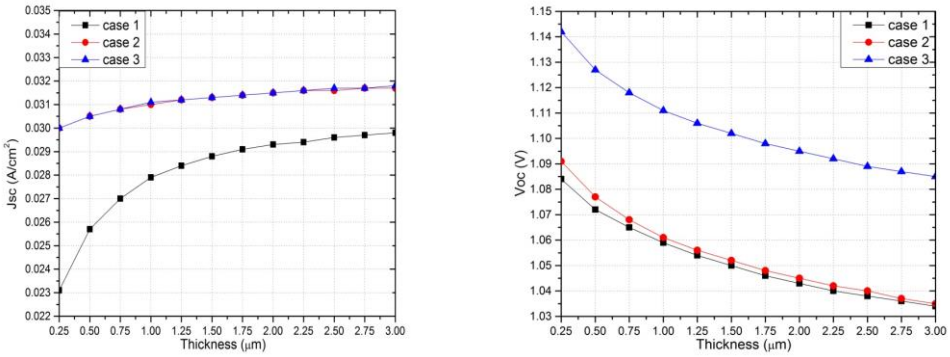

Fig. 3.3 J_{sc} vs. Thickness and V_{oc} vs. Thickness

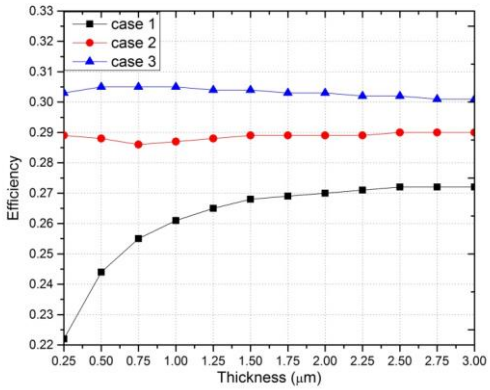

Fig. 3.4 The Efficiency changes with thickness

From J_{sc}-Thickness curves, J_{sc} is significantly increased when the rear reflector is applied but there is no large difference between different B values. J_{sc} increases as the increase in rear reflection leads to more absorbed light. The open circuit voltage does not change significantly when the rear reflection changes but the impact of photon recycling causes a big increase in V_{oc}. Photon recycling will increase the effective minority carrier lifetime and facilitate the separation of quasi-Fermi level and therefore will increase V_{oc}.

V_{oc} increases as thickness of the active layer decreases which can be explained from the following equation:

$$V_{oc} \approx \frac{kT}{q} ln(\frac{J_{sc}}{J_0}) \approx \frac{kT}{q} ln(\frac{J_{sc} N_D \tau_{eff}}{q n_i^2 d}) \quad (3.2)$$

A thinner layer ($d\downarrow$) can reduce the recombination levels and so the dark saturation current density J_o, so it will increase V_{oc}.

3.3 Photon recycling calculating model

The effects of photon recycling were further studied by Myles A. Steiner et al. [38] and a photon recycling model was built whose structure is shown in Fig. 3.5. The geometry for modeling of the photon recycling is shown in Fig. 3.5 where the optical emission is from a single junction solar cell with the active thickness L and frontal area A. The colored lines (red, green and blue) represent the different processes that an emitted photon experienced in the GaAs solar cells: red line shows the emitted photon is re-absorbed at $\vec{r}$ after one reflection at the front; the green dashed line shows the diffusion of electron-hole pair; the blue line represents that an emitted photon escapes after twice internal reflection at $\vec{r'}$. The purple lines demonstrate the Fresnel reflection at the front and rear surface. P_{esc} and P_{abs} represent the probability densities of escape out the front and of re-absorption, respectively, respecting an initial emission in the differential volume element dv. The front reflectance is $R_f = 1 - T_f = \begin{cases} 0: \theta < \theta_c \\ 1: \theta > \theta_c \end{cases}$, where the critical angle θ_c is defined by $sin\theta_c = \frac{1}{n}$ and n is the refractive index of GaAs. This model

calculates the probabilities of escape out the front and of re-absorption in the GaAs solar cell structure, integrated over the cell volume, the solid angle of emission, and the distribution over energy.

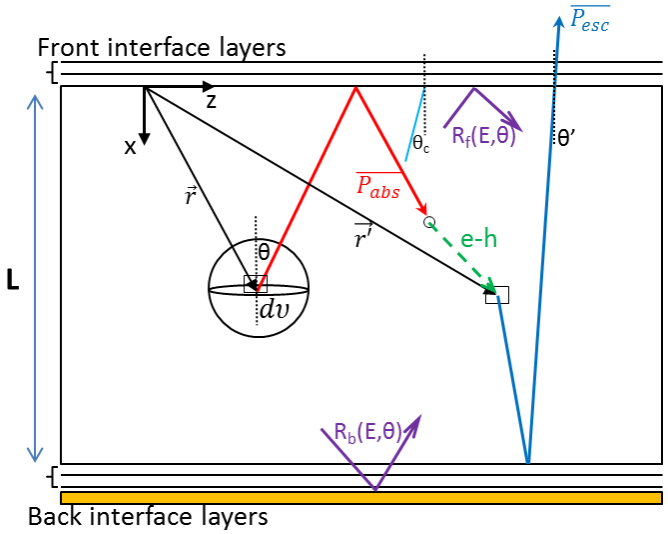

Fig. 3.5 Geometry for modeling photon recycling [38]

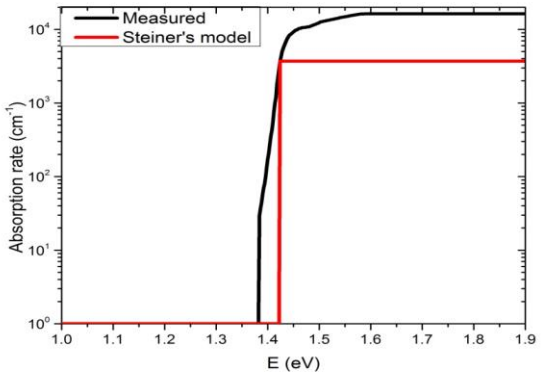

Fig. 3.6 Absorption rate of GaAs

In Steiner's model, a step function of absorption rate was used. Here, a measured absorption rate [39] is applied as shown in Fig. 3.6. First, the spontaneous emission distribution [40] needs to be calculated with the following expression:

$$S(E) = \frac{2\alpha(E)n^2(E)E^2}{h^3c^2}\frac{1}{exp\left(\frac{E-qV}{kT}\right)-1} \tag{3.3}$$

where, α(E) is the absorption coefficient of the absorber layer, *n(E)* is the refractive index of the absorber layer, and *V* is the bias voltage. When $E - qV \gg kT$, *S(E)* can be re-written as

$$S(E) \approx \frac{2\alpha(E)n^2(E)E^2}{h^3c^2} exp\left(\frac{-E}{kT}\right) exp\left(\frac{qV}{kT}\right) \tag{3.4}$$

Integrating *S(E)* over all the energies, the normalized spontaneous emission distribution is

$$\hat{S}(E) = \frac{\frac{2E(E)n^2(E)E^2}{h^3c^2} exp\left(\frac{-E}{kT}\right) exp\left(\frac{qV}{kT}\right)}{\int_0^\infty S(E)dE} \tag{3.5}$$

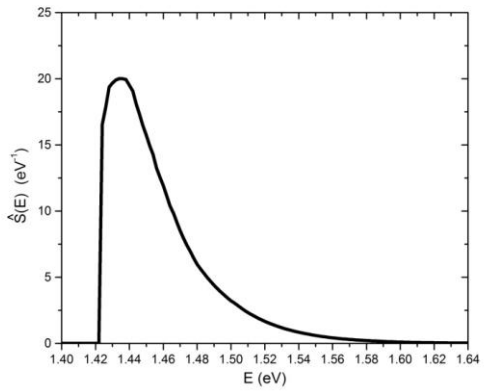

Fig. 3.7 Normalized spontaneous emission distribution

The probability of a particular photon escaping out of the front is given by:

$$\overline{P_{esc}} = \int_0^{\infty} \hat{S}(E) \int_0^{\pi/2} \frac{T_f}{2\alpha L} \frac{\left(1-e^{-\frac{\alpha L}{cos\theta}}\right)(1+R_b e^{-\frac{\alpha L}{cos\theta}})}{1-R_f R_b e^{-\frac{2\alpha L}{cos\theta}}} cos\theta \, sin\theta \, d\theta \, dE \tag{3.6}$$

The probability of a particular photon being reabsorbed is given by:

$$\overline{P_{abs}} = 1 - \int_0^{\infty} \hat{S}(E) \int_0^{\pi/2} \frac{\left(1-e^{-\frac{\alpha L}{cos\theta}}\right)}{\alpha L} \left(1 - \frac{1}{2}\left(1-e^{-\frac{\alpha L}{cos\theta}}\right) \frac{R_f+R_b+2R_f R_b e^{-\frac{2\alpha L}{cos\theta}}}{1-R_f R_b e^{-\frac{2\alpha L}{cos\theta}}}\right) cos\theta sin\theta d\theta dE \tag{3.7}$$

More detailed derivation calculation can be found in Steiner' paper [38]. Fig. 3.8-3.10 display the calculation results.

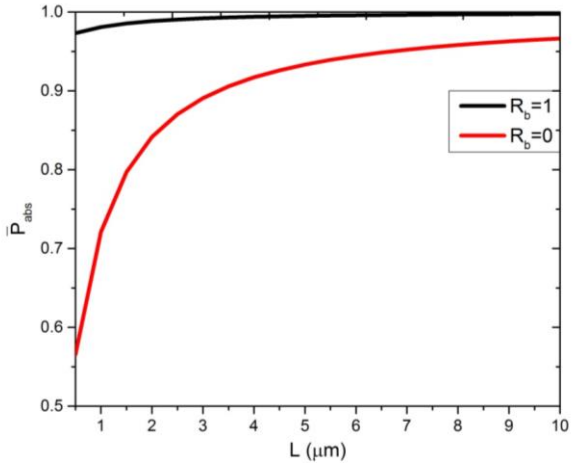

Fig. 3.8 Re-absorption probability $\overline{P_{abs}}$

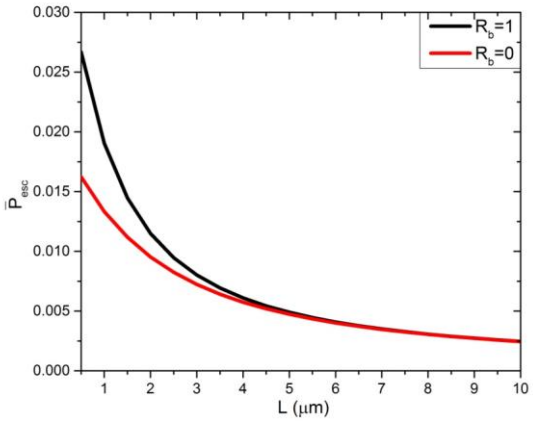

Fig. 3.9 The probability of photons escaping from front $\overline{P_{esc}}$

The external luminescent efficiency η_{ext}:

$$\eta_{ext} = \frac{\eta_{int}\overline{P_{esc}}}{1-\eta_{int}\overline{P_{abs}}} \tag{3.8}$$

where, η_{int} is the internal luminescent efficiency which is given by

$$\eta_{int} = \frac{R_{rad}}{R_{rad}+R_{nr}} \tag{3.9}$$

where, R_{rad} and R_{nr} are the radiative and non-radiative recombination rates, respectively.

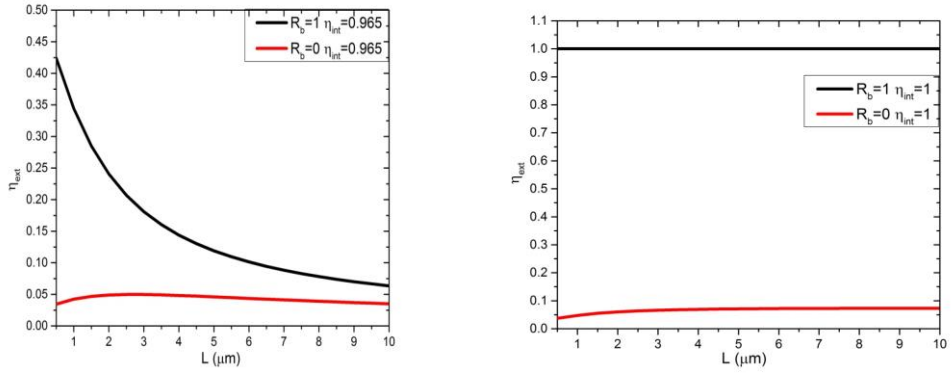

Fig. 3.10 External luminescent efficiency η_{ext} with different rear reflector and different η_{int}

From this model the effective radiative coefficient can be calculated according to the relationship: $B = (1 - \eta_{int}\overline{P_{abs}}) \times B_0$, where B_0 is the intrinsic radiative coefficient and the value used here is $5 \times 10^{-10} cm^3/s$ according to [39]. The calculation result is shown in Fig. 3.11

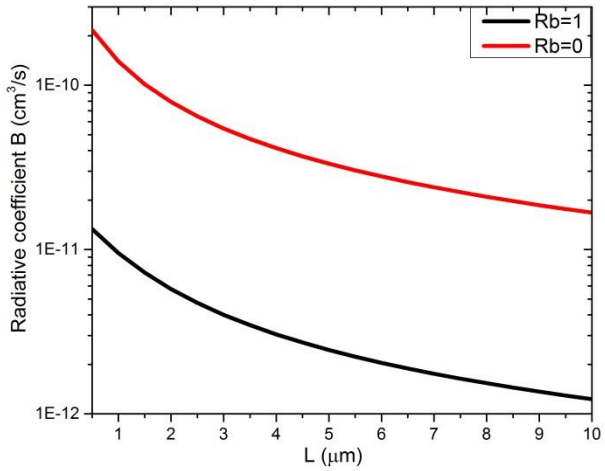

Fig. 3.11 Radiative coefficient at the condition of η_{int}=1

3.4 GaAs solar cells simulation using PC1D

In this section the new photon recycling model which is modified from Steiner's model is applied into the PC1D simulation by calculating the effective radiative recombination. The best record single junction solar cell is reported in 2012 [30], however, the specifications of the cell have not been reported. A reasonable structure [41] as shown in Fig. 3.12 shown and doping levels are shown in Table 3.1.

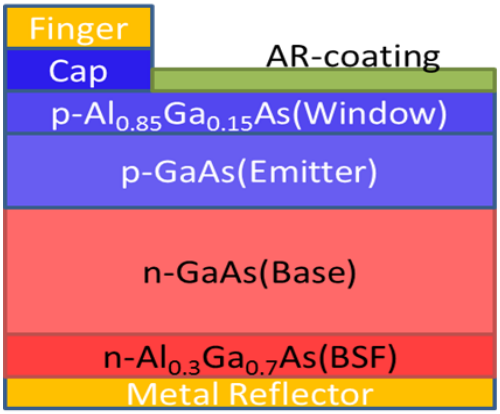

Fig. 3.12 Simulated structure for GaAs thin solar cells [41]

Table 3.1 Thickness and doping density for every epilayer

Layer	Thickness(μm)	Doping Density(cm^{-3})
Window	0.03	3×10^{18}
Emitter	0.15	1×10^{18}
Base	1.5	2×10^{17}
BSF	0.02	4×10^{18}

The calculated effective radiative coefficient B is $1.12\times10^{-11}cm^3/s$ using the photon recycling model assuming rear reflector is 95% and $\eta_{int}\approx1$. The SRH lifetime is assumed to be 1μs and the Auger coefficient is $7.0\times10^{-30}cm^6/s$ according to the literature [42].The front reflectance loss is assumed to be 6.5% and the internal front surface reflectance is assumed to be 96.9%. The front contact is assumed to be 0.7Ω and the rear contact of 0.4Ω to match FF reported by Alta Devices [30]. The front and rear recombination of S_r=50cm/s is used. With these assumptions, the simulation results

closely match the efficiency of the record cell [30]. The V_{oc}, J_{sc} and η are reduced to 1.06V, 29.4mA and 26.7%, respectively, without considering the photon recycling caused by the reflector according to the simulation in PC1D compared to those with photon recycling shown in Table 3.2.

Table 3.2 Simulation result comparing to reference [30]

	Simulation result	**Alta Device(2012.05)**
V_{oc}(V)	1.122	1.122
J_{sc}(mA/cm^2)	29.7	29.68
FF	0.864	0.865
Efficiency	28.8%	28.8%

The effective lifetime under different light intensities ranging from 0.01 suns to 100 suns is simulated via PC1D and is shown in Fig. 3.13, which shows that the lifetime increases as the intensity reaches about 5 suns and then decreases with further increases in light intensity because of high recombination at the high injection level at high concentrated light. The effective lifetime changing with different injection levels is shown in Fig. 3.14.

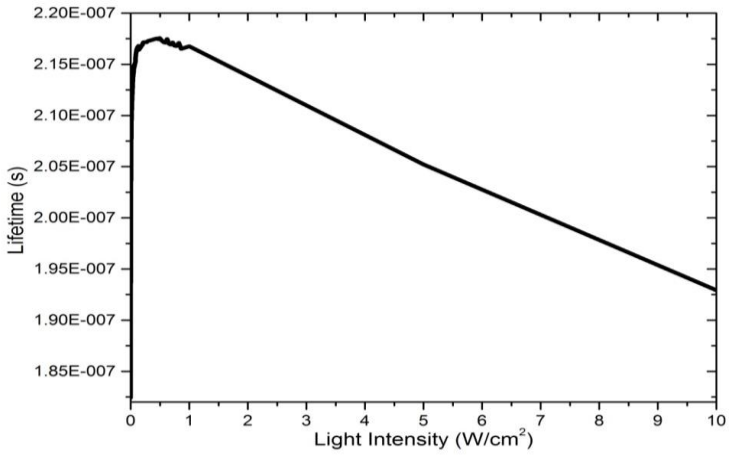

Fig. 3.13 Effective Lifetime with different light intensity

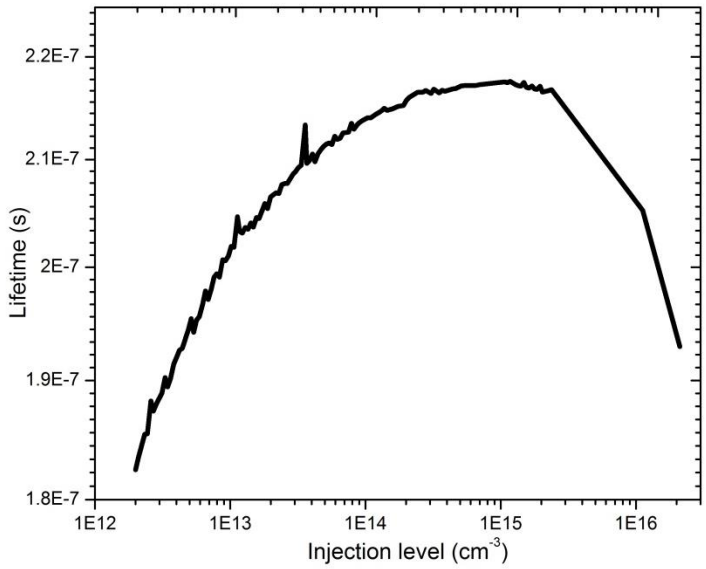

Fig. 3.14 Effective Lifetime with different injection level

Table 3.3 Calculated lifetime at the base layer at low injection level

Area	Doping/cm^{-3}	Effective τ_{rad}	τ_{SRH}	τ_{Auger}	τ_{bulk}
n-GaAs(1.5μm)	2×10^{17}	4.46×10^{-7}s	1×10^{-6}s	3.57×10^{-6}s	2.84×10^{-7}s

At the condition of low injection, the different lifetime mechanisms in the base layer are calculated as shown in Table 3.3, and the effective bulk lifetime at base layer is calculated by the following expression:

$$\frac{1}{\tau_{bulk}} = \frac{1}{\phi_{PR}\tau_{rad}} + \frac{1}{\tau_{SRH}} + \frac{1}{\tau_{Auger}} \tag{3.10}$$

The lifetime values in the Table 3.3 show that the radiative recombination is still dominant recombination which limits the effective bulk lifetime even after considering the photon recycling. Therefore, increasing the effective radiative recombination lifetime is still an approach to further improve the performance of GaAs solar cells.

CHAPTER 4

DEVICE FABRICATION

Figure 4.1 illustrates the fabrication processes for III-V solar cells. Solar cell growth, dielectric isolation, front and back electrical contacts and anti-reflection coating are the essential processes to fabricate a solar cell.

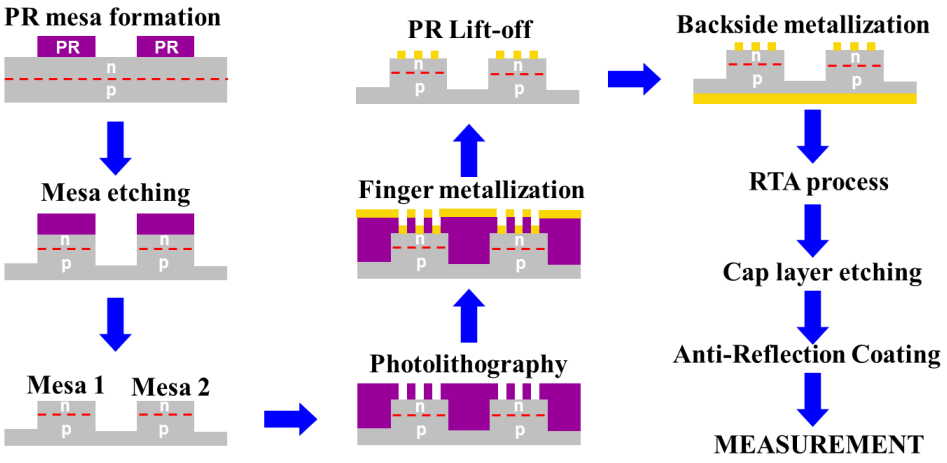

Fig. 4.1 Fabrication process flow for III-V solar cells

4.1 Wafer preparation

The solar cell growth contains two processes: one is to grow bulk single-crystal substrates by standard single crystal boule fabrication which is usually done by either Czeochralski method or float one and Bridgman alternatives, and the other process is to grow hetero- or homo-epitaxial films. Chemical vapor deposition (CVD) is commonly used to grow III-V semiconductor compounds. The most well-known CVD technique is atmospheric pressure metal organic vapor phase epitaxy (MOVPE) or metal organic

chemical vapor deposition (MOCVD) which is used for mass production due to the relatively low cost for material growth. MOCVD is an epitaxial growth technique in which the metal-organic precursor gases including dopant species impinge on a wafer that is placed on a temperature controlled stage, resulting in epitaxial growth whose rate at the order of microns per hour. Another epitaxial technique is molecular beam epitaxy (MBE) whose operation condition requires ultra-high vacuum (UHV). In contrast to MOCVD, for MBE the crystal-growth is performed by physical deposition rather than by chemical reaction. Overall, MOCVD is more used because of its relatively low cost and the monolayer control achievable in the best conditions.

Since different lattice constants of the grown layers give rise to strain, the lattice constant is an important hetero-generous growth consideration. The strain energy density increases as deposited layer thickness at the hetero-junction interface and when the deposited thickness is larger than Matthews-Blakeslee critical thickness limit [43], the strain energy becomes greater than the bond energy and the total system energy releases strain potential energy through breaking bonds in the interface. One solution to the lattice misfit problem is to grow relaxed buffer layers which allow the layer to relax and the dislocation density can be at reasonably low levels.

In this thesis, the wafers were grown by a commercial company using MOCVD and the structure is shown in Fig. 4.2. After the wafer fabrication, cell isolation and ohmic contact are two indispensable processes for solar cell fabrication.

To get rid of particles and contamination, wafers are cleaned with the following steps: a) Acetone rinsing for 3 minutes; b) Methanol rinsing for 3 minutes; c) DI-water rinsing; d) Nitrogen blow-off.

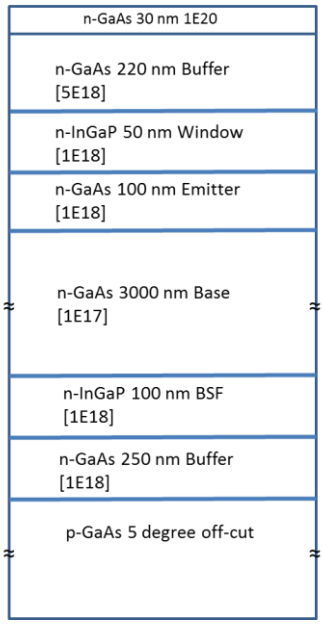

Fig. 4.2 The wafer structure of GaAs solar cell grown by MOCVD

4.2 Mesa etching process

In order to dielectrically isolate solar cells on the wafers, mesa etching is needed. As shown in Fig. 4.3, a photolithography for mesa formation is the first step in the mesa etching process. This process was done in the Center for Solid State Electronics (CSSER). After using spin-coating to form photoresist (AZ4330) coating on wafers, using a mask aligner to photolithography with ultra-violet (UV) and then developing process (AZ300MIF,~50 seconds), mesa patterns were achieved. The GaAs layer was etched using H_3PO_4:H_2O_2:DI water (1:1:3) at an etch rate of 25 nm/s at room temperature and

HCl solution etched InGaP layer for 30 seconds as shown in Fig. 4.4. The mesa etching process is completed when about half of the base layer thickness has been etched, followed by a deionized water rinsing and drying in N_2 flow.

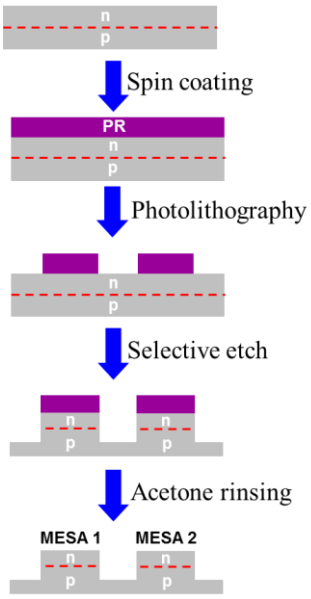

Fig. 4.3 Illustration of mesa etching process

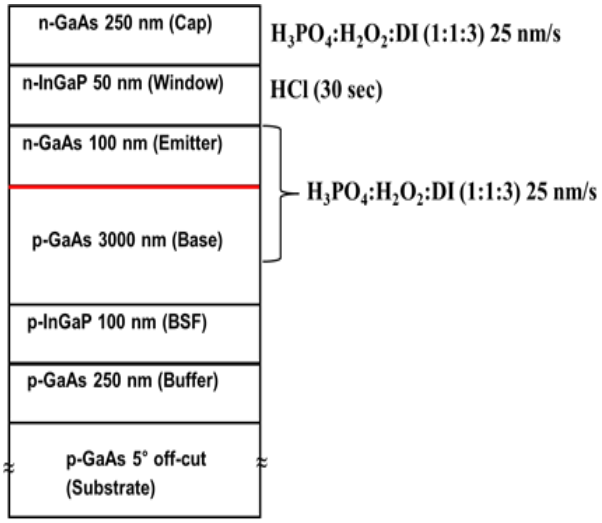

Fig. 4.4 Selective etch for GaAs-based solar cells

4.3 Metallization

To make a semiconductor device, metal contacts have to be made which leads to metal-to-semiconductor (M-S) contacts. The behavior of these junctions depends on the work functions and the energy band structures of the constituent materials. The work functions of a variety of metals are shown in Table 4.1. In the electronic contact formed by metal and semiconductor, the Fermi levels will line up by the exchange of charge carriers across the junction, with the consequence that the layers approach the thermal equilibrium. As shown in Fig. 4.5, band bending behavior appears as electrons density changes and the Schottky barrier height ϕ_m is formed at the interface of metal and semiconductor. In order to achieve ohmic behavior and "free" movement of the charge carriers across the M-S junction, the band bending and work function difference should be reduced. Four possible metal-semiconductor junction configurations and the resulting contact type are shown in Table 4.2 according to analysis of band bending behavior and carriers flowing. However, contact metals may react with or diffuse into semiconductor surface, which leads to the formation of a compound with new electronic properties in the real condition.

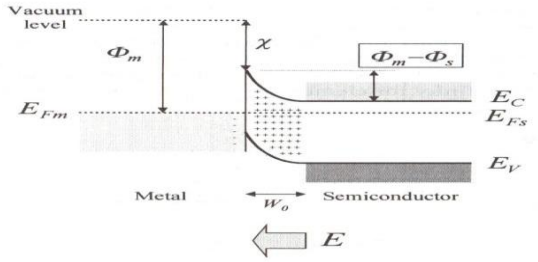

Fig. 4.5 Schematic band diagram of a typical Metal-Semiconductor Junction [44]

Table 4.1 Work Functions of Selected Metals [45]

Material	Face	Work Function(eV)
Li	Polycrystal	2.9
Na	Polycrystal	2.75
K	Polycrystal	2.3
Rb	Polycrystal	2.16
Cs	Polycrystal	2.14
Al	(1 0 0)	4.41
	(1 1 0)	4.06
	(1 1 1)	4.24
Ag	(1 0 0)	4.64
	(1 1 0)	4.52
	(1 1 1)	4.74
Cu	(1 0 0)	4.59
	(1 1 0)	4.48
	(1 1 1)	4.98
Au	(1 0 0)	5.47
	(1 1 0)	5.37
	(1 1 1)	5.31
W	(1 0 0)	4.63
	(1 1 0)	5.25
	(1 1 1)	4.47
Ni	(1 0 0)	5.22
	(1 1 0)	5.04
	(1 1 1)	5.35
Mo	(1 0 0)	4.53
	(1 1 0)	4.95
	(1 1 1)	4.55

Table 4.2 Different Possible Metal-Semiconductor Junction Configurations

Junction Configuration	Semiconductor Doping	Junction type
$\varphi_M > \varphi_s$	n-type	Schottky
$\varphi_M < \varphi_s$	n-type	Ohmic
$\varphi_M > \varphi_s$	p-type	Ohmic
$\varphi_M < \varphi_s$	p-type	Schottky

The simple M-S contact theory presented in the previous section assumes that the electron affinities and work functions remain unchanged when the contact is made. However, the assumption is not true after considering the surface states at the metal-semiconductor interface [46]. In the reference [47]-[52], some theories and various mechanisms, including electronegativeity, have been developed, but no precise definite explanation has been made to explain the properties of metal and compound semiconductor contacts likely due to the lack of detailed information on the nature of M-S contacts on the atomic level and differences in deposition techniques for contact. In order to obtain ohmic contact for GaAs and other compound semiconductors, all electronic states should be filled or emptied [46]. There are two ways to accomplish this: one is heavily doping the semiconductor layer and the other one is diffusing metal from metal into semiconductor. Therefore, thermal processing of metallic layers, like annealing, is a crucial process. A cap layer is needed to protect the epitaxial layers from being damaged by the deep diffusion of metals. Generally, a heavily doped cap layer will

be applied to achieve good ohmic contact. The following metallization for n- and p-type was completed in the clean room of Solid State Electronics Research Center (CSSER) at ASU.

4.3.1 n-type Front metallization

The metals stack and layers thicknesses of the multilayer metallization for ohmic contact were selected according to literatures. Ge/Au/Ni/Au layers are chosen to be deposited on n-type front to form ohmic contact [46].

The following steps are for finger metallization are: a) Photoresist (AZ4330) coating using a spinner; b) Photolithography using a mask aligner; c) Developing process (AZ300MIF, ~50 sec). N-contact metal deposition using a thermal evaporator Ge/Au/Ni/Au (260/540/150/1500Å) and lift-off process using Acetone are two processes to achieve finger metallization (n-type ohmic contact).

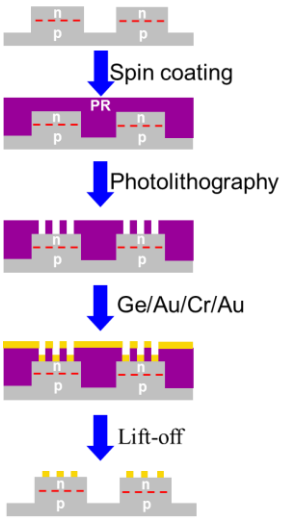

Fig. 4.6 Illustration of n-type front metallization

4.3.2 p-type Backside metallization

The Ti/Pt/Au [54] system is commonly used for p-type rear ohmic contacts. GaAs surfaces tend to lose arsenic during contact formation, and thus a diffusion barrier like Ti or Ni is often used to reduce As loss.

Using a photo resist (AZ4300) coating on the front to protect finger, Ti/Pt/Au (40/10/1500Å) is deposited using E-beam evaporator. After removing the photo resist using Acetone, the backside metallization is completed.

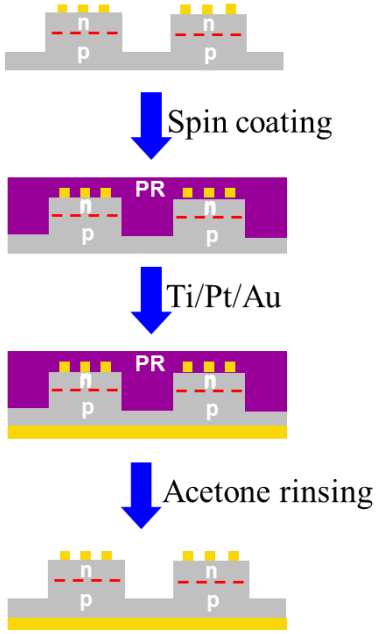

Fig. 4.7 Illustration of p-type backside metallization

4.3.3 Rapid Thermal Annealing (RTA)

After depositing metals on the front and rear side of solar cells, rapid thermal annealing (RTA) is required for achieving ohmic contact. The I-V curve of the surface shown in Fig. 4.8 is called double Schottky diodes behavior.

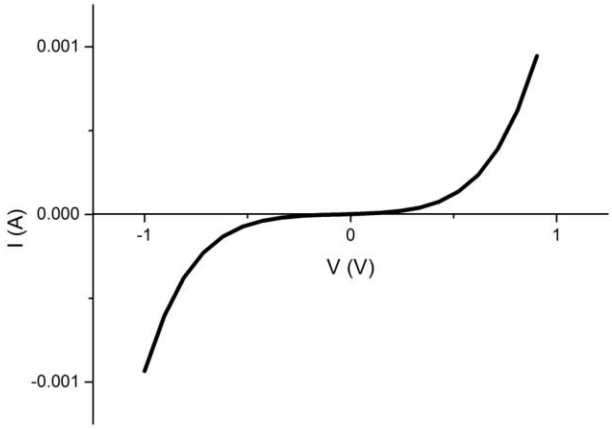

Fig. 4.8 I-V curve of surface contact without RTA process showing non-ohmic behaviors

Transmission line measurements (TLM), which were originally proposed by Shockley [55] to determine specific-contact resistivity, are used to find optimized annealing temperature and annealing time so that minimum contact resistance of solar cells can be achieved.

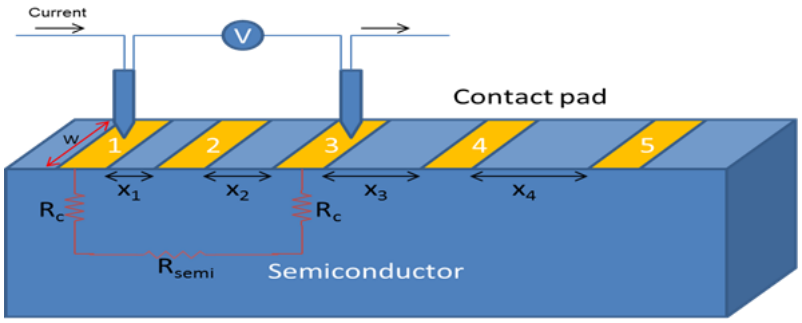

Fig. 4.9 Schematic transmission line measurement

As shown in Fig. 4.9, TLM measurements are performed by a probe station with a parameter analyzer like HP4145 after metals are patterned and annealed by different recipes. A voltage between several pairs of adjacent pads in a row is applied, and the I-V curves are measured. The design of TLM patterns requires all the pads in one row, the pads are the same size, and the distance between pads is varied. Figure 4.10 shows the TLM patterns used in this experiment.

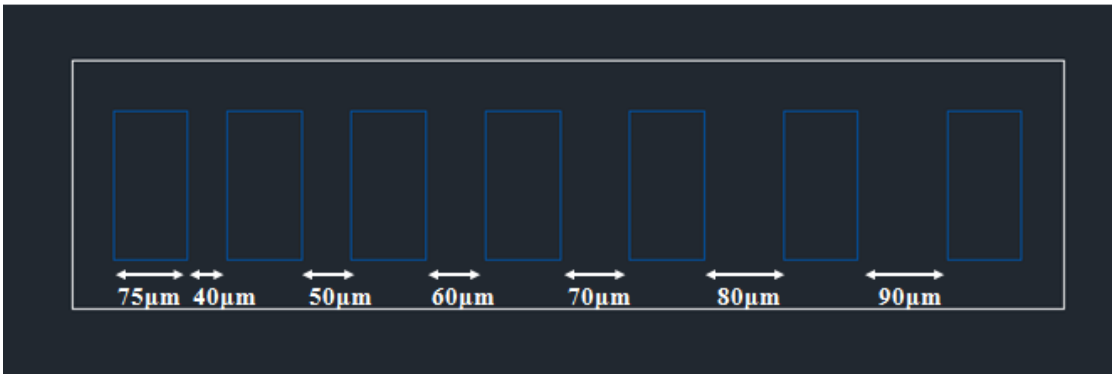

Fig. 4.10 The structure of TLM patterns used in the experiment

The resistances between two pads are calculated by $R=V/I$ which is a total resistance $R_{total}=2R_c+R_{semi}$, where R_c is contact resistance and R_{semi} is the semiconductor resistance. By measuring of the resistance between metal pads for a set of different gaps,

the total resistance according to the contact separation is plotted in Fig. 4.11. After the linear fitting of R_{total} vs. contact separation, sheet resistance of semiconductor can be obtained by equation $R_{sheet}=slope\times w$, where w is the width of pattern which is shown in Fig. 4.9 and contact resistance can be got from equation $R_c=0.5\times intercept$. The specific contact resistivity can be calculated by $\rho_c=R_c\times A$, where A is the contact pad area.

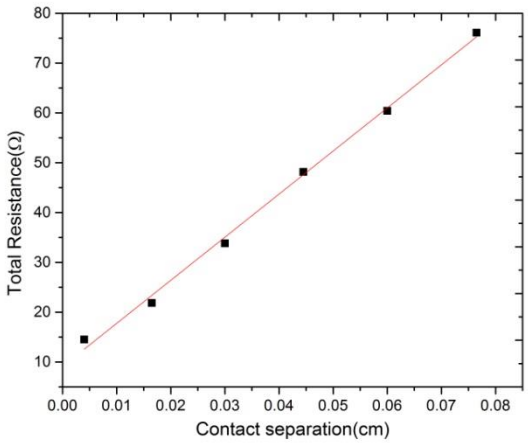

Fig. 4.11 The total resistance at different pad positions of one pattern and linear fitting

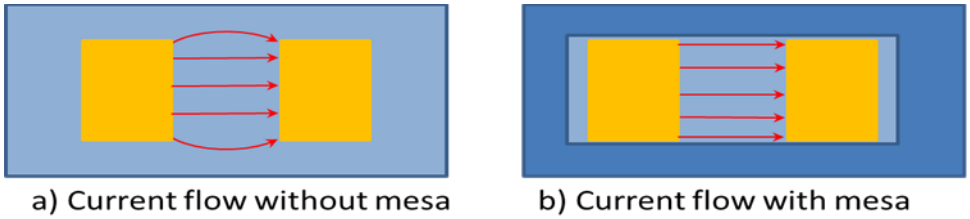

Fig. 4.12 The schematic of TLM patterns with and without mesa etching

As shown in Fig. 4.12, the TLM pattern with mesa etching has better uniformity in current flow. In this optimization process, the patterns do not have mesa etching

process, leading to the result with some noise. In order to certify almost the same conditions, the same wafer and same depositing process are used in comparing annealing temperature varying from 320-380℃, 380-440℃ for 20s, and annealing time from 20s to 50s at 380℃. From Fig. 4.13, the specific contact resistivity seems not to have big difference at the annealing time from 360-440℃ for 20s. In addition to changing RTA temperatures, different annealing times of 20s and 50s at a fixed RTA temperature of 380℃ is compared as shown in Fig. 4.14. These results show longer annealing times have lower contact resistivity. Therefore, an RTA temperature of 380℃ for 50s is an optimum condition among these different conditions for n-type ohmic contact.

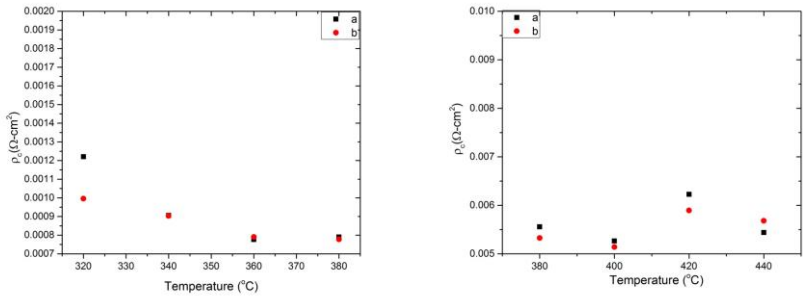

Fig. 4.13 The specific contact resistivity at different annealing temperature for 20s (two row patterns are measured)

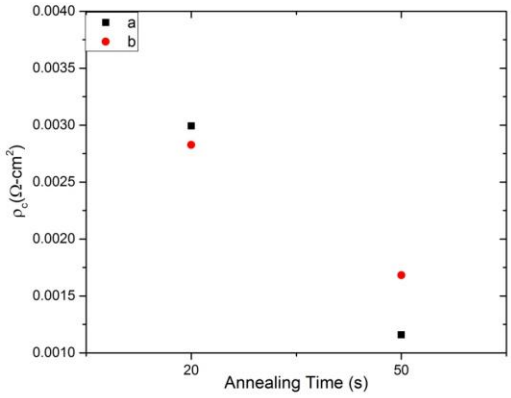

Fig. 4.14 The specific contact resistivity with different annealing time at the RTA temperature of 380℃ (two row patterns are measured)

The front n-type contact is studied in the previous section. Here different annealing temperatures are compared for p-type contact using TLM as shown in Fig. 4.15 that 380℃ for 50s is better than 400℃ for 50s. Therefore, the RTA condition for n-type and p-type contact of the wafers used in this thesis is 380℃ for 50s. All the RTA processing was done in the Solar Power Lab of ASU.

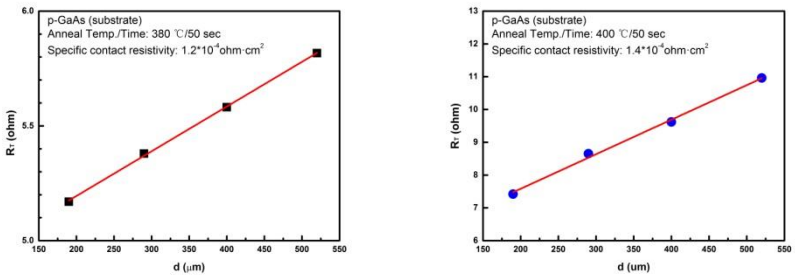

Fig. 4.15 p-type contact results of TLM

4.4 Cap layer etching

The top GaAs cap layer is heavily doped and there are two functions for the cap layer on the window layer: one is to protect a window layer and the other is to be used for electric contact layer. After finishing ohmic contacts for front and rear side, the EQE spectra are shown in Fig. 4.16, where the light with short wavelengths is absorbed at a cap layer. Therefore, the cap layer needs to be etched out from a window layer using H_3PO_4: H_2O_2: DI water (1:1:3) for ~10s which was completed in Solar Power Lab.

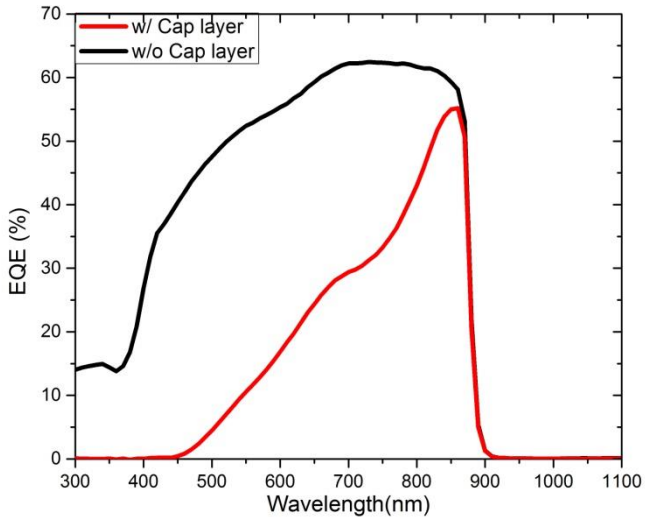

Fig. 4.16 The EQE spectra with and without a cap layer

4.5 Anti-reflection coating (ARC)

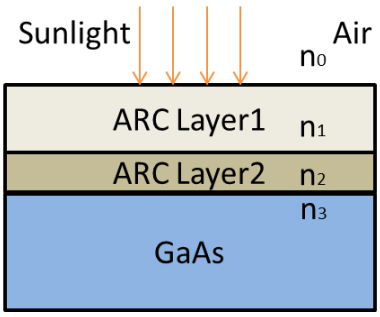

Fig. 4.17 The structure of ARC on GaAs

Reducing the optical losses is a key to achieving high efficiency solar cells. The reflection on the GaAs solar cells without antireflection coatings is very high, more than 30% according to the equation [56]: $R = (\frac{n_1 - n_0}{n_1 + n_0})^2$. It is not sufficiently effective to have a single layer coating for GaAs solar cells because the single layer coating only can effectively reduce the reflection in a narrow wavelength range. In other words, the single layer just can realize the minimization of one wavelength. Two or more anti-reflection coating layers are generally required to get better transmittance. An alternative is a graded-index coating which the refractive indices increase from small to large from the air. Therefore, double layers antireflection coatings (DLARC) which contain low and high refractive indices are necessary to get further reflectivity decrease.

There are two advantages to deposit two layers rather than single layer: first, two reflection minima can be achieved which helps to lower the average spectral-weighted reflection rate; second, the optical performance is less sensitive to the thickness variations [57]. The most popular DLARC in GaAs based solar cells are zinc sulfide

(ZnS)/magnesium fluoride (MgF_2).

Considering normal incidence of light, the surface reflection at a specific wavelength can be minimized when the refractive indexes meet the following relation:

$$\frac{n_0}{n_1} = \frac{n_1}{n_2} = \frac{n_2}{n_3} \tag{4.1}$$

The refractive index of GaAs is 3.82 at a wavelength of 650nm [58]. The value of n_3 is 3.82, therefore, the optimized n_1 is 1.56 and n_2 is 2.44 as calculated through Equation 4.1.

The reflection of DLARC can be calculated through the equations below:

$$r_i = \frac{n_{i-1}-n_i}{n_{i-1}+n_i}, \text{ where } i=1,2,3 \tag{4.2}$$

$$\theta_j = \frac{2\pi n_j t_j}{\lambda}, \text{ where } j=1,2 \tag{4.3}$$

$$R = \frac{\sum_1^3 r_i^2+\prod_1^3 r_i^2+2r_1r_2(1+r_3^2)cos2\theta_1+2r_2r_3(1+r_1^2)cos2\theta_2+2r_1r_3cos2(\theta_1+\theta_2)+2r_1r_2^2r_3cos2(\theta_1-\theta_2)}{1+r_1^2r_2^2+r_1^2r_3^2+r_2^2r_3^2+2r_1r_2(1+r_3^2)cos2\theta_1+2r_2r_3(1+r_1^2)cos2\theta_2+2r_1r_3cos2(\theta_1+\theta_2)+2r_1r_2^2r_3cos2(\theta_1-\theta_2)} \tag{4.4}$$

where, n_0 is the refractive index of the surrounding region, n_1 is the refractive index of the first layer of ARC and t_1 is the thickness, n_2 is the refractive index of the second layer of ARC and t_2 is the thickness.

To calculate the optimized combinations of refractive indexes and thicknesses for the incident spectrum, the average weighted reflection should be calculated using the equation [59] below:

$$R_w = \frac{\int_{\lambda_{min}}^{\lambda_{max}} R(\lambda)N_{ph}(\lambda)\,d\lambda}{\int_{\lambda_{min}}^{\lambda_{max}} N_{ph}(\lambda)\,d\lambda} \tag{4.5}$$

where, $R(\lambda)$ is the wavelength-dependent reflection, $N_{ph}(\lambda)$ is the photon flux of the AM1.5 (or AM0 for space use) solar spectrum as a function of the wavelength.

Suitable materials with low refractive index around 1.56 are SiO_2, Al_2O_3, and MgF_2, and the materials with high refractive index around 2.44 are ZrO_2, ZnS, and TiO_2. All refractive index data is from [58].The minimum R_w is achieved in the range of 300 - 900 nm as shown in Table 4.3. The minimum R_w of SiO_2/TiO_2 layers for DLARC is as low as 1.23%, therefore, these two materials are further studied in this thesis.

In this thesis the DLARC SiO_2/TiO_2 films are deposited by e-beam evaporator in CSSER. The refractive index of SiO_2 and TiO_2 deposited by E-beam evaporator is affected significantly by the deposition conditions [60]-[62] such that , to a certain degree, the higher vacuum in the chamber, the higher substrate temperature of the substrate, and the faster growth rate, the higher refractive index can be obtained. Through some experiments, the refractive index of SiO_2 is approximately 1.45, and that of TiO_2 is ranges from 2.2 to 2.4.

Table 4.3 Simulation results using different material groups

	ARC Layer1	ARC Layer2	Optimum Thickness/nm		
Theoretical Refractive Indices (λ=650nm)	1.56	2.44	Layer1	Layer2	*minimization of* R_w
Suitable materials (λ=650nm)	SiO_2(n=1.54)	ZrO_2(n=2.205)	66	51	3.07%
	SiO_2(n=1.54)	ZnS(n=2.55)	85	51	1.21%
	SiO_2(n=1.54)	TiO_2(n=2.57)	85	51	1.23%
	Al_2O_3(n=1.658)	ZrO_2(n=2.205)	57	45	3.79%
	Al_2O_3(n=1.658)	ZnS(n=2.55)	75	46	2.1%
	Al_2O_3(n=1.658)	TiO_2(n=2.57)	76	46	2.02%
	MgF_2(n=1.377)	ZrO_2(n=2.205)	89	60	2.02%
	MgF_2(n=1.377)	ZnS(n=2.55)	98	54	1.24%
	MgF_2(n=1.377)	TiO_2(n=2.57)	98	54	1.28%

On a GaAs substrate, 50nm TiO_2 under the conditions of 5.5×10^{-5}Torr vacuum, deposition rate of 0.06nm/s and substrate temperature of 300℃ and 90nm SiO_2 under the conditions of 4.8×10^{-7}Torr vacuum, deposition rate of 0.1nm/s and substrate temperature of 78℃ are deposited using an E-beam evaporator. A weighted reflection of 1.9% at a wavelength range from 400-900nm is achieved in contrast to that of 29.7% without antireflective coating, as shown in Fig. 4.18.

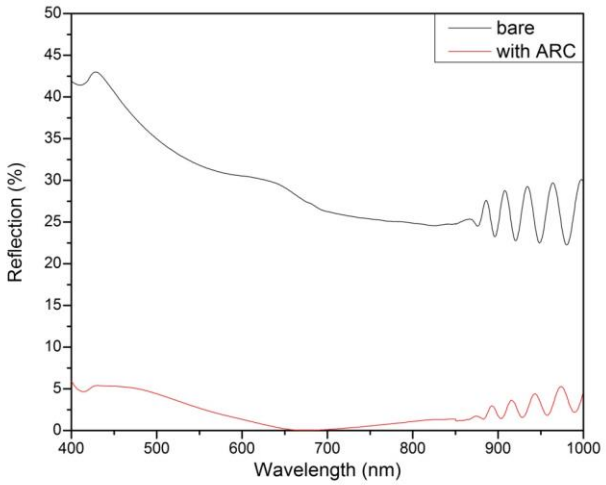

Fig. 4.18 The reflection spectra with and without ARC on GaAs wafers

Considering that 300℃ for more than 1 hour may damage GaAs based solar cells, for the final solar cell fabrication, anti-reflection coatings were deposited at room temperature rather than 300℃ and the result will be shown in Chapter 5.

CHAPTER 5

MATERIAL CHARACTERIZATION

In this chapter, two kinds of GaAs wafers with different growth rates grown by MOCVD are compared (Fig. 5.1) from a commercial company. The slow growth rate is 14μm/hour and fast growth rate is 55μm/hour. Two wafers are prepared for slow growth (slow-1 and slow-2) and fast growth (fast-1 and fast-2).

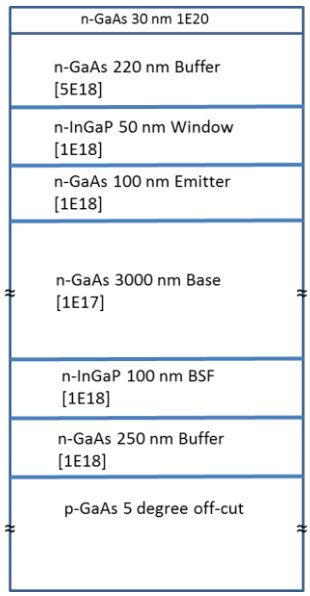

Fig. 5.1 The structure of GaAs solar cell wafers grown by MOCVD

5.1 Crystalline Quality

The as-grown samples are characterized by high-resolution X-ray diffraction (HRXRD) to determine layer composition, strain, and crystalline quality. X-ray is well suited for analyzing epitaxial thin sloar cells deposited on single-crystal substrates because the wavelength of X-ray is comparable with the inter spacing (10^{-8}cm) in crystals.

The X-ray rocking curve which is the plot of X-ray intensity against the X-ray incident angle Omega is taken from two cuts of the Ewald sphere [63] in the reciprocal space as shown in Fig. 5.2. In Fig. 5.2 **hkl** is the Miller indices of the plane on the crystal and **s** is the diffraction vector. GaAs and InGaP both have the zinc blend crystal structure. When the diffracted angle 2θ=66.05 ° with copper X-ray source, according to Bragg's law $\lambda=2d_{hkl}\sin\theta$ and intensity calculation from structure factor, the X-ray beam hits on the (004) planes of GaAs can produce the highest diffraction peak. Therefore, the diffraction measurement is in the vicinity of (004) planes.

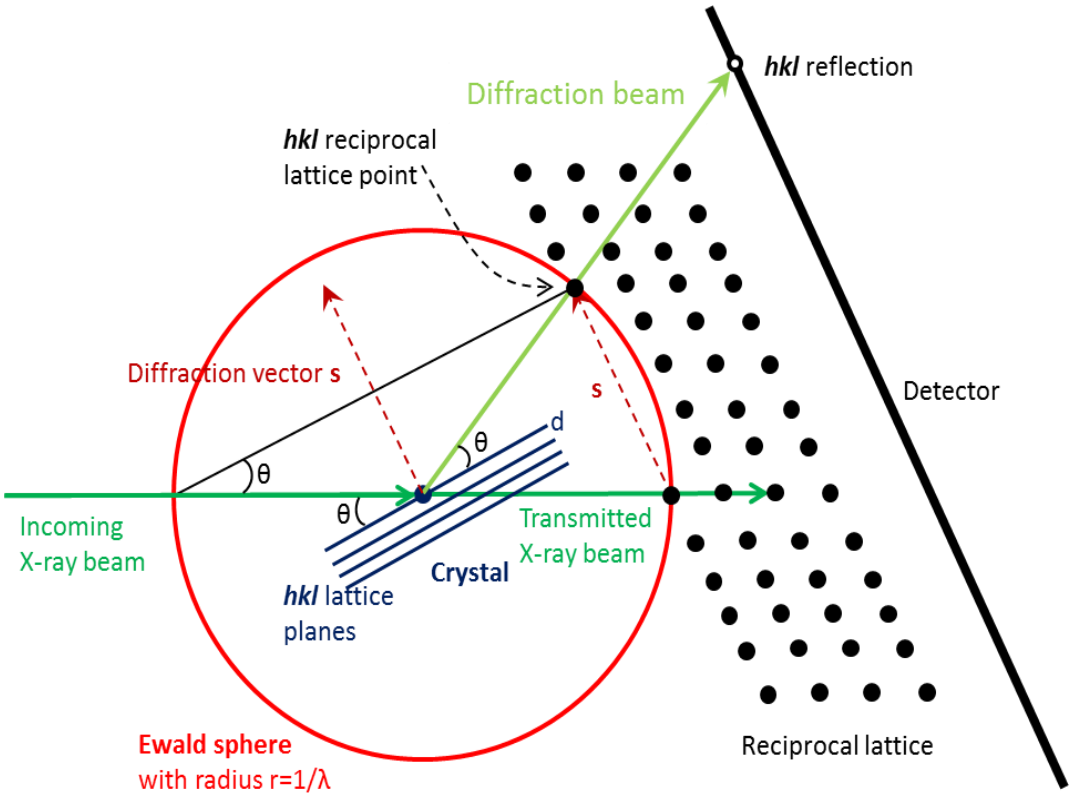

Fig. 5.2 Schematic Ewald's sphere construction applied in XRD measurement

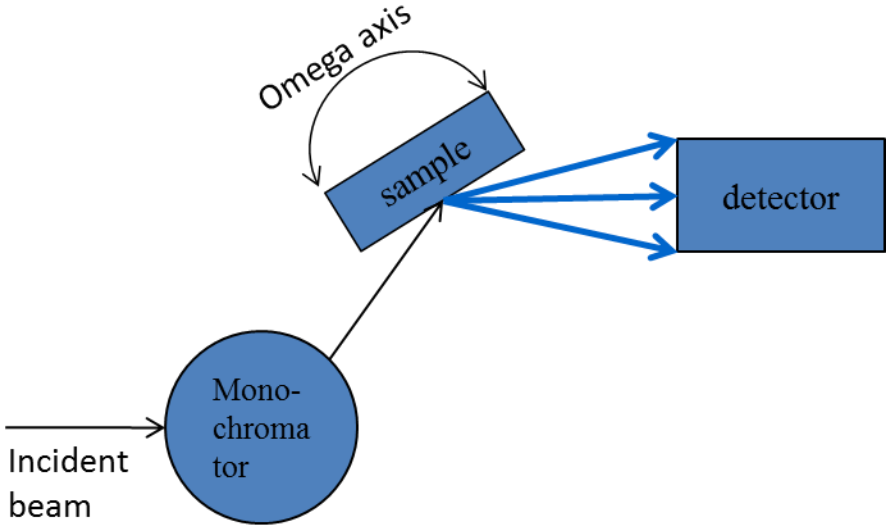

Fig. 5.3 Schematic double-crystal (DC) rocking curves (RC) measurement

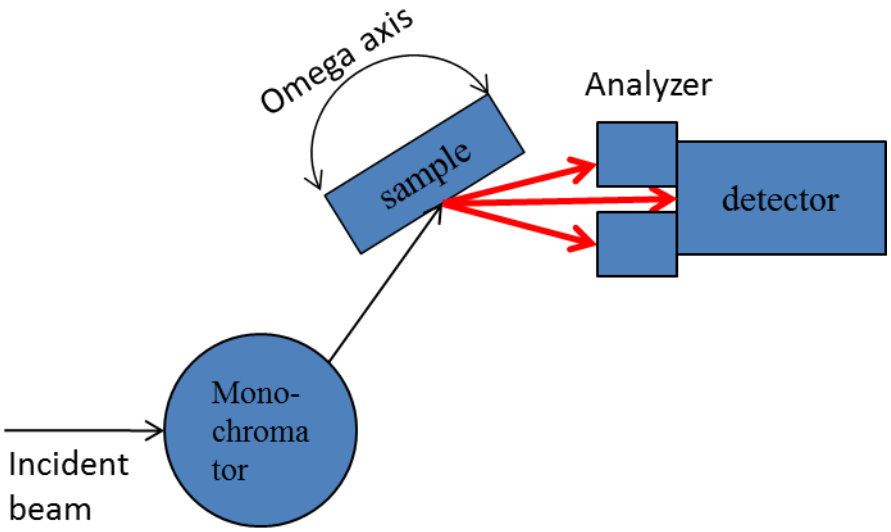

Figure 5.4 Schematic triple-crystal (TC) rocking curves (RC) measurement

There are two instrumental configurations for HRXRD, double-crystal and triple-crystal rocking curves measurement, as shown in Fig. 5.3 and Fig. 5.4, respectively. The

XRD measurement was done in LeRoy Eyring Center for Solid State Science. In double-crystal rocking curves measurements, the sample is rotated about its omega axis changing the incident angle and all Bragg angles are measured simultaneously over a limited range, so more peaks are observed. The analyzer constrains the detector and only one special peak is observed in triple-crystal rocking curves measurement.

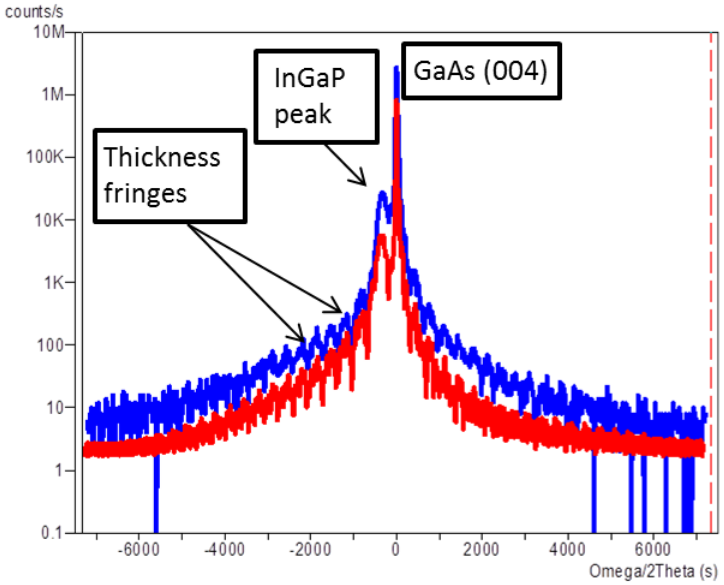

Fig. 5.5 Double-crystal (DC) ω-2θ rocking curves (RC) of Sample slow-1 in the vicinity of (004) reflection (**Blue**– Experimental, **Red** – Calculated)

From the rocking curves, the peak position can give the d-spacing for the Bragg peak which will provide the information on anything that changes the lattice parameter of the unit cell, such as composition or strain/relaxation. The width of the epitaxial film's Bragg peak can be used to quantify the film thickness and the thickness fringes can also be used to quantify the film thickness. From the double-crystal rocking curve and doing

calculations as shown in Fig. 5.5, the different layer thickness and composition (from substrate to top layers) of Sample slow-1 can be achieved:

Substrate, thick = 600.00 μm, GaAs, (0 0 1), Strain = 0.0

Layer 1: thick = 0.0040 μm, $Ga_{0.495}In_{0.505}As_{0.2}P_{0.8}$, Strain = 8382ppm, R% = 0.0

Layer 2: thick = 0.1060 μm, $Ga_{0.4975}In_{0.5025}P$, Strain = 1241ppm, R% = 0.0

Layer 3: thick = 0.0020 μm, $GaAs_{0.8}P_{0.2}$, Strain = -7188ppm, R% = 0.0

Layer 4: thick = 3.200 μm, GaAs, Strain = 0ppm, R% = 0.0

Layer 5: thick = 0.0040 μm, $Ga_{0.495}In_{0.505}As_{0.2}P_{0.8}$, Strain = 8382ppm, R% = 0.0

Layer 6: thick = 0.0530 μm, $Ga_{0.4995}In_{0.5005}P$, Strain = 1093ppm, R% = 0.0

Layer 7: thick = 0.00200 μm, $GaAs_{0.8}P_{0.2}$, Strain = -7188ppm, R% = 0.0

Layer 8: thick = 0.1920 μm, GaAs, Strain = 0ppm, R% = 0.0

From the double crystal (DC) rocking curves (RCs) in Fig. 5.6, the highest peaks come from GaAs layers and the second highest peaks are from InGaP layers. The different positions of InGaP peak indicate the different indium composition in InGaP layers. The indium composition, strain and epi-thickness in InGaP layers are calculated and displayed in Table 5.1. The different thicknesses may be due to the stage temperature variations during the wafer growing process using MOCVD.

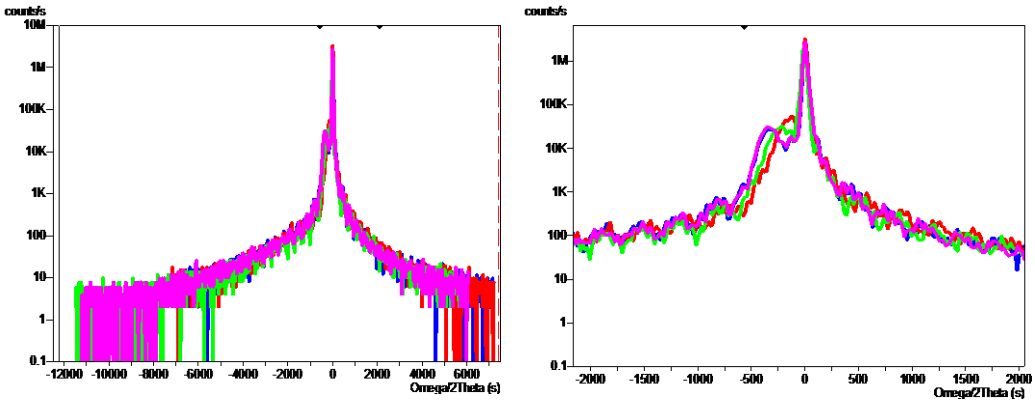

Fig. 5.6 Double-crystal (DC) ω-2θ rocking curves (RC) in the vicinity of (004) reflection (**Blue**– slow-1, **Red**– fast-1, **Green**– slow-2, and **Violet**– fast-2)

Table 5.1 Indium composition, strain and epi-thickness from the DC rocking curves

Sample	In (%)	Strain (ppm)	Thickness (nm)
slow-1	50.05	1,093	53
fast-1	49.55	723	55.5
slow-2	49.7	834	56
fast-2	50.22	1,219	58.5

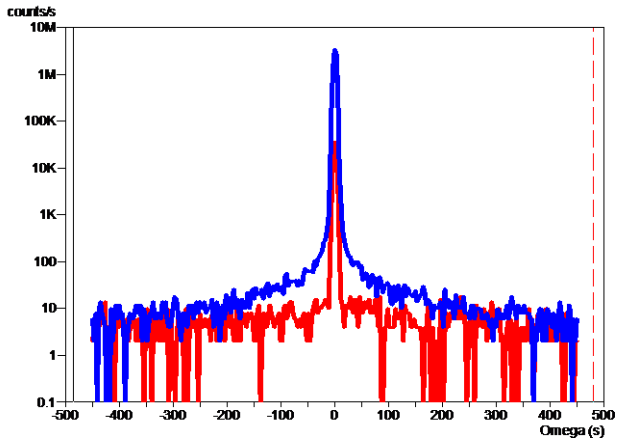

Fig. 5.7 Triple-crystal (TC) ω rocking curves (RC) of Sample slow-1 (**Blue**– Substrate peak (004) Reflection, **Red**– GaInP peak)

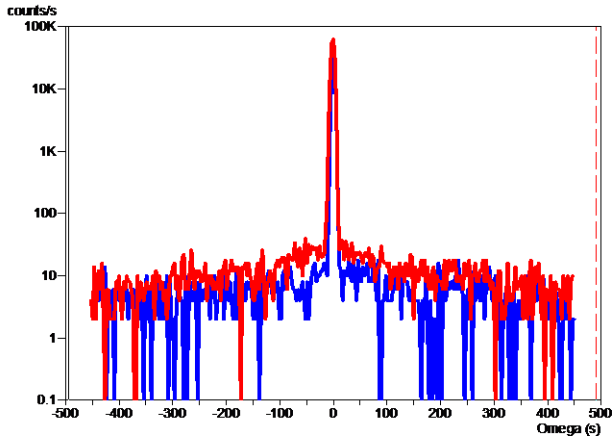

Fig. 5.8 TC ω rocking curves (RC) of Sample slow-1(**red**) and Sample fast-1(**blue**) at InGaP peak

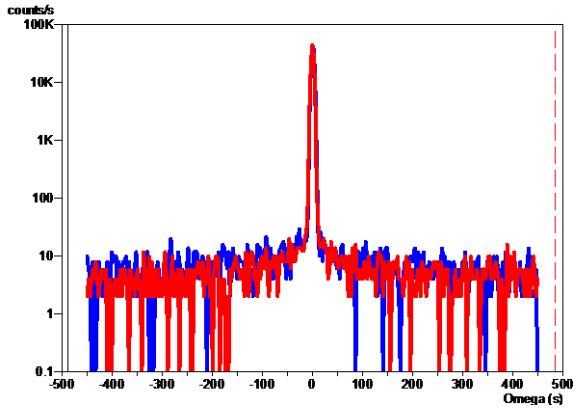

Fig. 5.9 TC ω rocking curves (RC) of Sample slow-2 (**blue**) and Sample fast-2 (**red**) at InGaP peak

Calculating the full width at half maximum (FWHM) of peaks is a path to estimate defects in crystals. A perfect crystal will produce a very sharp peak with an intrinsic width. Defects such as dislocation cause peak broadening at the Bragg angles. Dislocations are lines along which the crystal pattern is broken in single crystals. But in general, dislocations appear in curves or loops, which in three dimensions form and interlocking dislocation network. In Fig. 5.7, the TC ω rocking curve of Sample slow-1 is compared to that of substrate. The density of primary dislocation loops (DLs) in Sample slow-1 $\leq 10^4/cm^2$, and in Sample fast-1, it is about $4 - 6.4 \times 10^4/cm^2$ from Fig.5.8. The more intense wide diffuse base on Sample fast-1 RC suggests more secondary DLs in the volume of InGaP layer(s). From Fig. 5.9, the density of DLs in Sample slow-2 is not more than $3.5 \times 10^4/cm^2$, and in Sample fast-2 it is about $1.5 \times 10^4/cm^2$.

Table 5.2 The DLs for solar cell wafers grown at different growth rates

Sample	Density of Dislocation Semi-Loops
slow-1	$\leq 10^4/cm^2$
fast-1	$\sim 4 - 6.4 \times 10^4/cm^2$
slow-2	$\leq 3.5 \times 10^4/cm^2$
fast-2	$\sim 1.5 \times 10^4/cm^2$

Therefore, from Table 5.2, the density of DLs for these slow and fast growth wafers is on the same level. The crystal quality of the fast growth wafers is not degraded from XRD analysis.

5.2 Solar cell characterization

The as-grown wafers are fabricated into solar cells using the processes described in Chapter 4. The size of the fabricated solar cells is 0.5cm×0.5cm. The optical and electrical properties of the fabricated solar cells of Sample slow-2 (slow growth) and Sample fast-2 (fast growth) are compared. Surface reflection, EQE, dark current and Suns-V_{oc} were measured in the Solar Power Lab.

5.2.1 Surface reflection

The surface reflection of the solar cells affects the intensity of the incoming light beam that gets into cells. 56nm TiO_2 and 90nm SiO_2 are deposited onto the GaAs solar

cells surface by E-beam evaporator at room temperature. As shown in Fig. 5.10, the surface reflection is quite high without anti-reflective coating (ARC) whose weighted reflection is more than 33%. The reflection on the cells is about 8% which contains the reflection of fingers on the surface. From the reflection curves, the conclusion can be made that there is no big difference between the slow and fast growth solar cells and some slight difference may be caused by a little difference of layer thickness and indium composition. Therefore, nearly the same surface reflection for both cells is confirmed.

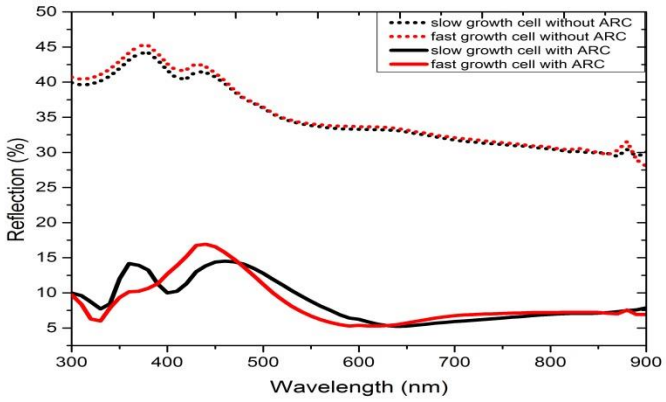

Fig. 5.10 Surface reflection spectra

Table 5.3 The weighted reflection R_w in the wavelength region of 300-900nm

Before ARC		After ARC	
slow	fast	slow	fast
33.56%	33.87%	8.2%	8.1%

5.2.2 External quantum efficiency (EQE)

The external quantum efficiency (EQE) is the ratio of the number of carriers collected by the solar cell and to the number of photons from a given light incident on the solar cell. EQE at each wavelength of the light is defined by

$$EQE = \frac{\#electrons/second}{\#photons/second} = \frac{1240\ nm/eV \times (J_{light} - J_{dark})}{\lambda \times P_{light}} \tag{5.1}$$

There is some difference between 600nm to 880nm for slow growth and fast growth solar cells as shown in Fig. 5.11.

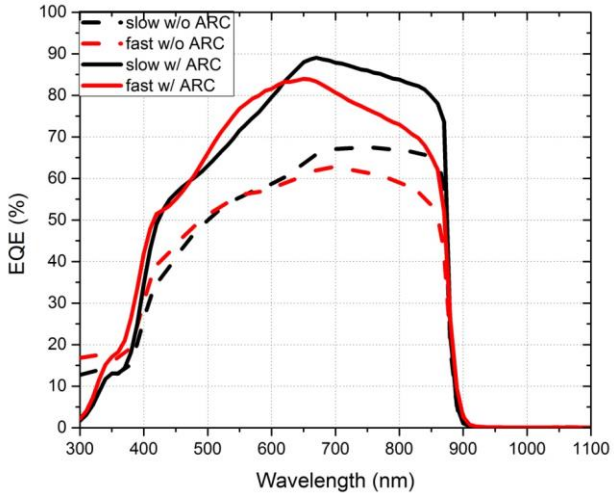

Fig. 5.11 EQE spectra of the slow and fast growth cells

The average EQE can be calculated by using the following equation:

$$EQE_{avg} = \frac{\int_{\lambda_{\min}}^{\lambda_{\max}} EQE(\lambda) N_{ph}(\lambda)\, d\lambda}{\int_{\lambda_{\min}}^{\lambda_{\max}} N_{ph}(\lambda)\, d\lambda} \tag{5.2}$$

From the EQE spectra, J_{sc} can be estimated by:

$$J_{sc} = q * \int_{\lambda_{min}}^{\lambda_{max}} EQE(\lambda) N_{ph}(\lambda)\, d\lambda \qquad (5.3)$$

As shown in Table 5.4, both average EQE and the solar cell with fast growth are lower than those of the slow growth solar cell.

Table 5.4 The average EQE and estimated J_{sc} for the slow and fast growth cells

	slow growth		fast growth	
	EQE_{avg}	Jsc(mA/cm^2)	EQE_{avg}	Jsc(mA/cm^2)
without ARC	54.30%	18.3	51.73%	17.4
with ARC	70.55%	23.7	67.42%	22.7

In order to investigate the cause for EQE difference in the wavelength region between 600nm and 880nm, some PC1D simulations are carried out. The radiative lifetime in the base layer is assumed to be 0.5μs corresponding to a radiative coefficient of $2.0 \times 10^{10} cm^{-3}/s$. From the simulation results shown in Fig. 5.12-5.13, when the thickness of base layer decreases and the SRH lifetime decreases in the base layer, the EQE decreases in the wavelength range of 600-880nm. The reason why fast growth cells have lower EQE in the wavelength range of 600nm-900nm may be due to lower SRH lifetime caused by increased crystalline defects. The surface/interface recombination difference may be also a reason for different EQE. More discussion will be carried out after analyzing the I-V data under 1.5AM spectrum.

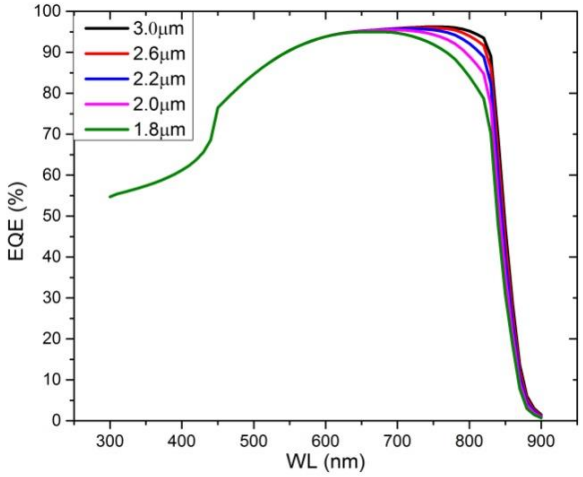

Fig. 5.12 EQE spectra for base layer with different thickness

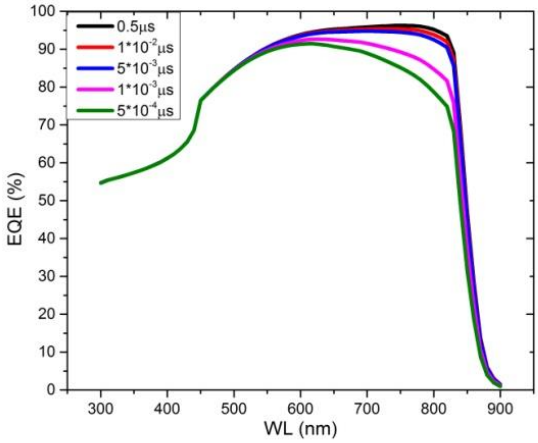

Fig. 5.13 EQE spectra for base layer with different SRH lifetime

5.2.3 Dark current

The dark I-V is measured to examine the diode rectifying properties under dark condition. In the dark, solar cells are working as a large flat diode and the I-V curves show exponential behaviors with the applied voltage as seen in Fig. 5.14(a).

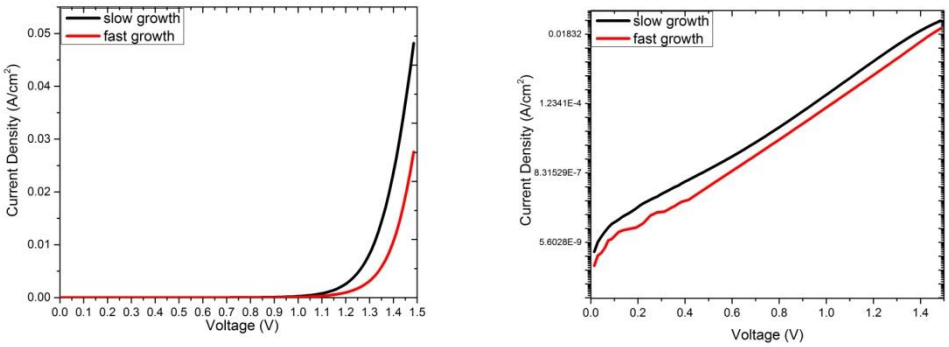

(a) Dark I-V on a linear scale (b) Dark I-V on a semilog scale

Fig. 5.14 Dark current

The dark saturation current J_0 and ideality factor n are obtained by the following equation:

$$ln(J) = ln(J_0) + (\frac{q}{nkT})V \quad (5.4)$$

where J is the dark current density, kT/q is the thermal voltage, and V is the bias voltage. The calculated results are listed in Table 5.5 where the ideality factor of slow growth is slightly larger than that of fast growth and also for J_0.

Table 5.5 Diode parameters of the cells from the linear fitting and calculation from dark I-V

	Slow growth	Fast growth
Intercept	-19.685	-20.865
J_0(A/cm^2)	2.8×10^{-9}	8.7×10^{-10}
Slope	11.3655	11.6146
Ideality factor	3.40	3.33

5.2.4 Suns-Voc

The *Suns-V_{oc}* [64] is a measurement that directly measures V_{oc} as a function of the light intensity, typically measured ranging from a few suns to just below 0.1 suns as shown in Fig. 5.15. In contrast to dark I-V measurement, the *suns-V_{oc}* follow the dark current curve but it has no effects of series resistance. The local ideality factor, *m*, can be derived from the following equation [65]:

$$suns \cdot J_{sc} = J_0 exp(\frac{qV_{oc}}{mkT}) \quad (5.5)$$

where, *suns* is the light intensity, J_{sc} is the short circuit current density of the cell at one sun, and J_0 is the dark saturation current density.

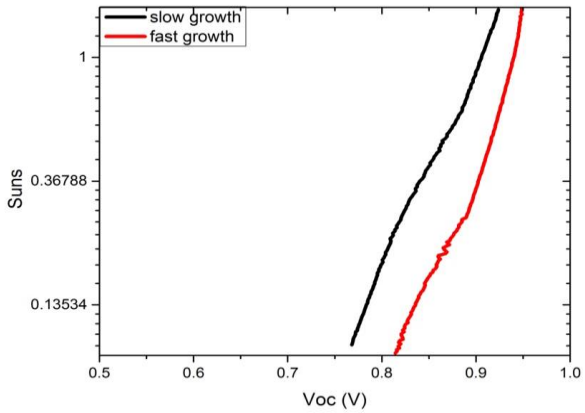

Fig. 5.15 *Suns*-V_{oc} curves against V_{oc} on a semilog scale

Table 5.6 Ideality factors calculated from *Suns*-*Voc* curves

	Slow growth	Fast growth
intercept	-14.62	-18.01
slope	16.158	19.04955
Ideality factor	2.39	2.03

From Table 5.6, local ideality factor of slow growth cell is larger than that of fast growth cell which is consistent with the calculated result from the dark I-V data.

5.2.5 I-V under AM1.5 spectrum

The measurement of the conversion efficiency of solar cells is a fundamental characterization technique for solar cells. The solar simulator whose lamp is simulating air mass 1.5 spectrum (AM1.5) with the illumination intensity of 100mW/cm^2 is

employed to simulate standard sun light on earth surface. The cells are measured at room temperature and the I-V curves shown in Fig. 5.16. The J_{sc} increases significantly after anti-reflective coating and V_{oc} slightly increases.

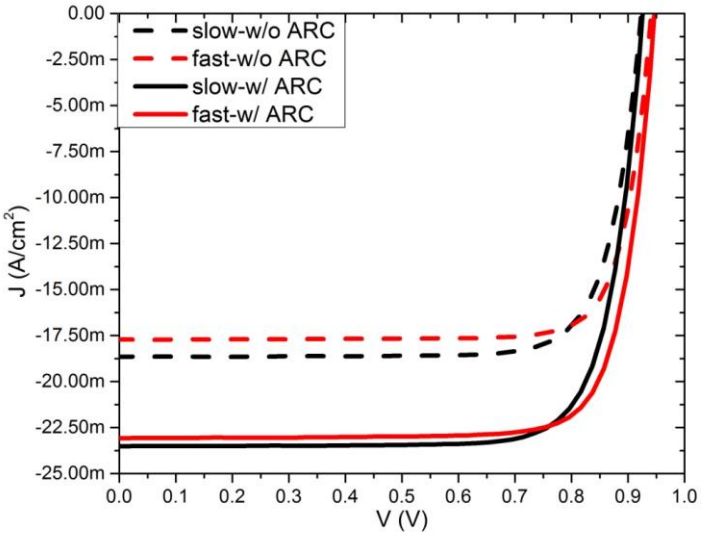

Fig. 5.16 I-V curves of slow growth and fast growth

The shunt resistance and series resistance can be estimated [66] from the I-V curves by calculating $R_{sh}=dV/dI$ at V=0 and $R_s=dV/dI$ at I=0. The TLM patterns on the wafers are measured to extract the sheet resistance and specific contact resistivity in Fig. 5.17. The sheet resistance of the slow growth wafer is slightly lower than that of fast growth wafer and the specific contact resistivity for both wafers is almost same in this study.

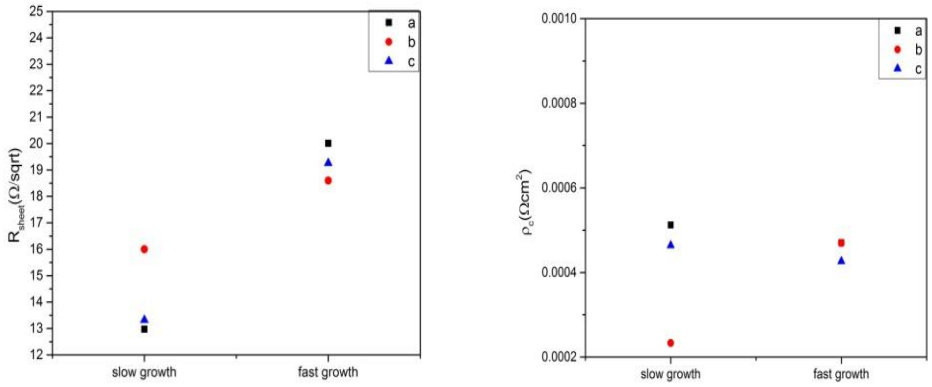

Fig. 5.17 Sheet resistance (R_{sheet}) and specific contact resistivity (ρ_c) measured from the TLM patterns on the surface of solar cells (a, b, and c indicate three patterns at different positions of the wafers)

From Table 5.7, the fill factors of the cells of slow growth and fast growth are close, and both are about 80%. The internally measured efficiency of both cells is above 17%. The shunt resistance R_{sh} and series resistance R_s are also shown in Table 5.7, where the calculation is based on the linear simulation to get slope at the V=0 and J=0, respectively. The current density J_{sc} of the slow growth cell is higher than that of the fast growth cell, while the open circuit voltage of the fast growth cell is higher than that of slow growth cell. As shown in the simulation result of Fig. 3.3, the thinner base layer, the higher V_{oc} and the lower J_{sc} can be obtained. The simulation of the structure shown in Fig. 5.1 result shows that if the lifetime goes to 5ns and 1ns without considering the interface recombination, the open circuit voltage is 0.9611V and 0.9111V, respectively simulated by PC1D. Therefore, the base thickness of fast growth solar cells may not be well

calibrated or/and there is large interface recombination that cannot be ignored. Lifetime measurement is needed to further investigate the difference between fast and slow growth solar cells.

Table 5.7 Device performances of the slow and fast growth cells

	Slow growth (w/o ARC)	Slow growth (w/ ARC)	Fast growth (w/o ARC)	Fast growth (w/ ARC)
J_{sc}/mAcm^{-2}	18.7	23.5	17.7	23.1
V_{oc}/V	0.923	0.926	0.941	0.947
FF/%	79.2	79.0	81.5	80.0
Efficiency/%	13.65	17.2	13.59	17.5
R_{sh}(Ω-cm^2)	2941.2	5443.7	8333.3	3736.9
R_s(Ω-cm^2)	3.0	2.4	2.6	3.0

CHAPTER 6

CONCLUSION

6.1 Summary

In this thesis, the different recombination mechanisms such as surface recombination, radiative recombination and non-radiative recombination are described. The effect of photon recycling in GaAs solar cells is studied via building a photon recycling model and PC1D simulation. The photon recycling plays a vital role in approaching the detail balance limit. The model of photon recycling is built by modifying the Steiner's model. This model is successfully applied to the simulation of the world record single-junction GaAs solar cell by assuming some boundary conditions. In addition, the effect of the base layer thickness is discussed the less thickness of GaAs solar cells in the case of low surface recombination, the higher V_{oc} can be achieved. In the thin GaAs-based solar cells with a good mirror at the rear side, high V_{oc} can be obtained without sacrificing J_{sc} benefited from the light trapping and photon recycling.

The fabrication processes of GaAs solar cells are described, as the following steps: wafer fabrication, dielectric isolation, front and rear side metallization, RTA, cap layer etching, and anti-reflective coating. In order to achieve good ohmic contacts for GaAs solar cells, transmission line method (TLM) was used to optimize the annealing time and temperature. Some ARC simulation of different material groups using Matlab showed ARC effects on the surface reflection of GaAs materials. The double crystal anti-reflective coating (DLARC) of SiO_2/TiO_2 shows good anti-reflective effect in the

simulation, nevertheless, the refractive index of SiO_2 and TiO_2, especially for TiO_2 is sensitive to the deposition conditions such as chamber vacuum, substrate temperature and deposition rate.

To corroborate the modeling results studied here, two kinds of wafers grown at different growth rates of 14 μm/hour and 55 μm/hour by MOCVD are investigated in this work. By analyzing the device performances of the fabricated solar cells, the crystalline quality of the fast and slow growth rate do not show big difference confirmed by XRD measurements. The device performances of EQE, dark-current, suns-V_{oc}, and I-V under 1 sun were measured to compare the electrical properties of these two solar cell wafers. The EQE_{avg}, V_{oc}, J_{sc}, FF, and efficiency of the slow and fast growth cells with ARC are 70.55%/67.42%, 0.926/0.947V, 23.5/23.1mA, 0.79/0.80, 17.2%/17.5%, respectively. The different V_{oc} and J_{sc} between the two cells may be due to the difference of the bulk lifetime in the base layer or/and the interface recombination through PC1D simulation, nevertheless, the exact reasons need to be further investigated.

6.2 Future work

The thicknesses of the ohmic metallization for n-type and p-type contact have not been calibrated, and thus the calibration should be done to obtain higher fill factor. The ARC without heating the substrate is needed to be redesigned to achieve better ARC effect. In order to identify the reason for the difference in the device performances of the two different cells, the thickness of every epi-layer is necessary to be calibrated. The minority carrier lifetime of the fast and slow growth cells is also needed to be measured

and compared because it is one of the key factors determining the cell performances. In this work, the V_{oc} obtained after fabrication is much lower than theoretical value which is more than 1V and the reasons needs to be investigated in order to further improve GaAs solar cells performance.

REFERENCES

[1] G. Phipps, C. Mikolajczak and Terry Guckes, "Indium and Gallium: long-term supply", *Renewable Energy Focus*, Vol. 9, pp. 56, 58-59, Jul.-Aug., 2008.

[2] J.L. Gray, "The Physics of the Solar Cell" in *Handbook of Photovoltaic Science and Engineering*,2nd ed., A. Luque and S. Hegedus, Ed. John Wiley & Sons, 2011,pp. 82-129

[3] ASTM G173-03, "Standard tables for reference solar spectral irradiances: Direct normal and hemispherical on 37 °tilted surface," ASTM International (2003)

[4] H. C. Casey and E. Buehler, "Evidence for low surface recombination velocity on n-type InP," *Applied Physics Letter*, Vol. 30, pp. 247, 1977

[5] A. Ehrhardt, W. Wettling and A. Bett**, "**Transient photoluminescence decay study of minority carrier lifetime in GaAs heteroface solar cell structures," *Applied Physics A.*, Vol. 53, pp. 123-129, Aug. 1991

[6] N.L. Dmitruk, V.I. Lyashenko, A.K. Tereshenko and S.A. Spektor, "Investigation of surface recombination on epitaxial GaAs films," *Physics Status Solidi (A)*, Vol. 20, pp. 53, Nov. 1973

[7] D.B. Wittry, "Cathodoluminescence and impurity variation in Te-doped GaAs," *Applied Physics Letters*, Vol. 8, pp. 142, 1966

[8] L. Jastrzebski, J. Lagowski and H.C. Gatos, "Application of scanning electron microscopy to determination of surface recombination velocity: GaAs," *Applied Physics Letters*, Vol. 27, pp. 537,1975

[9] D. E. Aspnes, "Recombination at semiconductor surfaces and interfaces," *Surface Science*, Vol. 132, pp.406-421, 1983

[10] A. Heller, "Conversion of Sunlight into Electrical Power and Photoassisted Electrolysis of water in photoelectrochemical cells," Accounts of chemical research, Vol. 14 pp. 154-162,1981

[11] B.A. Parkinson, A. Heller and B. Miller, "Enhanced photoelectrochemical solar-energy conversion by gallium arsenide surface modification," *Applied Physics Letters*, Vol. 33, pp. 521, 1978

[12] R.J. Nelson, J.S. Williams, H.J. Leamy, B. Miller, H.C. Casey, Jr., B. Parkinson and A. Heller, "Reduction of GaAs surface recombination velocity by chemical treatment," *Applied Physics Letters*, Vol. 36 pp. 76, 1980

[13] E. Yablonovitch, R. Bhat, J. P. Harbison, and R. A. Logan, "Survey of defect-mediated recombination lifetimes in GaAs epilayers grown by different methods," Applied Physics Letters, Vol. 50, pp. 1197-9 Apr. 1987

[14] L. W. Molenkamp and H. F. J. van't Blik, "Very low interface recombination velocity in (Al,Ga)As heterostructures grown by organometallic vapor-phase epitaxy," *Journal Applied Physics*, Vol. 64, pp. 4253, 1988

[15] J. M. Olson, R. K. Ahrenkiel, D. J. Dunlavy, B. Keys and A. E. Kibbler. "Ultralow recombination velocity at $Ga_{0.5}In_{0.5}P$/GaAs heterointerfaces," *Applied Physics Letters* Vol. 55, pp. 1208, 1989

[16] G. H. Olsen, M. Ettenberg, and R. V. D'Aiello, "Vapor-grown InGaP/GaAs solar cells," *Applied Physics Letters*, Vol. 33, pp. 606-608, 1978

[17] L. Pavesi, M.Guzzi, "Photoluminescence of $Al_xGa_{1-x}As$ alloys," Journal of Appied. Physics, Vol. 75, pp. 4779-4842, May 1994

[18] I. Schnitzer, E. Yablonovitch, C. Caneau and T. J. Gmitter, "Ultrahigh spontaneous emission quantum efficiency, 99.7% internally and 72% externally, from AlGaAs/GaAs/AlGaAs double heterostructures," Applied Physics Letter, Vol. 62, pp. 131, 1993

[19] D.Z. Garbuzov, "Redadiation effects, lifetimes and probabilities of band-to-band transitions in direct A_3B_5 compounds of GaAs Type," *Journal of Luminesc*ence, Vol. 27, pp. 109-112, 1982

[20] W. Gerlach, H. Schlangenotto and H. Maeder, "On the radiative recombination rate in silicon," *Physica Status Solidi (A)***,** Vol. 13**,** pp. 277-283, 1972

[21] W. Shockley, W. T. Read, Jr., "Statistics of the Recombinations of Holes and Electrons," Physical Review Letters. Vol. 87, pp. 835, 1952

[22] P. Auger, "Sur les rayons β secondaires produits dans un gaz par des rayons X," *C.R.A.S.* Vol. 177, pp. 169-171, 1923

[23] R. N. Hall, G. E. Fenner, J. D. Kingsley, T. J. Soltys, and R. O. Carlson, "Coherent Light Emission From GaAs Junctions," *Physical Review Letters*, Vol. 9, pp. 366–369, Nov. 1962

[24] Zh. I. Alferov, V. M. Andreev, M. B. Kagan, I. I. Protasov and V. G. Trofim, "Solar-energy converters based on p-n $Al_xGa_{1-x}As$-GaAs heterojunctions," *Soviet Physics: Semiconductors*, Vol. 4, pp. 2047, 1971

[25] M.A.Green,K. Emery,Y.Hishikawa, and W.Warta, "Solar cell efficiency tables (version 31)," *Progress in Photovoltaic: Research and Applications*, Vol. 16, pp. 61–67, 2008.

[26] G.J. Bauhuis, P. Mulder, E.J. Haverkamp, J.C.C.M. Huijben, and J.J. Schermer, "26.1% thin-film GaAs solar cell using epitaxial lift-off," *Solar Energy Materials & Solar Cells* Vol. 93, pp. 1488, 2009

[27] F. Newman, D. Aiken; P. Patel, D. Chumney, I. Aeby, R. Hoffman, P. Sharps, "Optimization of inverted metamorphic multijunction solar cells for field-deployed concentrating PV systems," *Photovoltaic Specialists Conference (PVSC), 2009 34th IEEE* , Vol. 001611, pp. 7-12, Jun. 2009

[28] M.M.A.J. Voncken, J.J Schermer, A.T.J. van Niftrik, G.J. Bauhuis, P. Mulder, P.K. Lasrsen, T.P.J. Peters, B. de Bruin, A. Klaassen and J.J. Kelly, "Etching AlAs with HF for Epitaxial Lift-Off Applications," *Journal of The Electrochemical Society*, Vol. 151, G347-G352, 2004

[29] M.A. Green, K. Emery, Y. Hishikawa, and W. Warta, "Solar cell efficiency tables (version 36)," *Progress in Photovoltaic: Research and Applications*, Vol. 18, pp. 346, 2010.

[30] M. A. Green, K. Emery, Y. Hishikawa, W. Warta and E. Dunlop, "Solar cell efficiency tables (version 42)," *Progress in Photovoltaic: Research and Applications*, Vol. 21, pp. 827–837, Aug. 2013

[31] C. H. Henry, "Limiting efficiencies of ideal single and multiple energy gap terrestrial solar cells," *Journal of Applied Physics*, Vol. 51, pp. 4494, 1980

[32] W. Shockley, H. J. Queisser. "Detailed Balance Limit of Efficiency of p-n Junction Solar Cells," *Journal of Applied Physics*, Vol. 32, pp. 510, 1961

[33] W. van Roosbroeck and W. Shockley, "Photon-Radiative Recombination of Electrons and Holes in Germanium," *Physical Review*, Vol. 94, pp. 1558, 1954

[34] W. P. Dumke, “Spontaneous Radiative Recombination in Semiconductors,” *Physical Review,* Vol. 105, pp. 139, 1957

[35] V. Badescu and P. T. Landsberg, “Theory of some effects of phonon recycling in semiconductors,” *Semiconductor Science and Technology*, Vol. 8, pp. 1267, 1993

[36] P. Asbeck, “Self-absorption effects on the radiative lifetime in GaAs-GaAlAs double heterostructures,” *Journal of Applied Physics*, Vol. 48, pp. 820, 1977

[37] O. D. Miller, E. Yablonovitch, and S. R. Kurtz. “Strong Internal and External Luminescence as Solar Cells Approach the Shockley-Queisser Limit,” *IEEE Journal of Photovoltaics*, Vol. 2, pp. 303-311, Jul. 2012

[38] M. A. Steiner, J. F. Geisz, I. Friedman, D. J. Duda, and S. R. Kurtz. “Optical enhancement of the open-circuit voltage in high quality GaAs solar cells,” Journal of Applied Physics, Vol. 113, pp. 123109, 2013

[39] G. B. Lush, “Recombination and absorption in n-type gallium arsenide,” Ph.D. dissertation, Purdue Univ., West Lafayette, IN, 1992

[40] J. I. Pankove, *Optical Processes in Semiconductors*, New York: Dover Publications, Inc, 1975

[41] X. Wang, M. R. Khan, J.L. Gray, M. A. Alam, M. S. Lundstrom. “Design of GaAs Solar Cells Operating Close to the Shockley-Quesser Limit,” *IEEE Journal of Photovoltaics*, Vol. 3, pp. 737-744, 2013

[42] G. J. Bauhuis, P. Mulder, E. J. Haverkamp, J.C.C.M. Huijben, J.J. Schermer, “26.1% thin-film GaAs solar cell using epitaxial lift-off,” *Solar Energy Mater. Solar Cells*, Vol. 93, pp. 1488–1491, 2009

[43] J.W. Matthews and A.E. Blakeslee, “Defects in epitaxial multilayers: I. Misfit dislocations,” *Journal of Crystal Growth*, Vol. 27 pp. 118-125, 1974

[44] Manijeh Razeghi, *Fundamentals of Solid State Engineering*, Kluer Academic Publishers (2002)

[45] J. I. Gersten and F. W Smith, *The Physics and Chemistry of Materials*, Wiley (2001)

[46] P. Karbownik, A. Baranska, A. Szerling, W. Macherzynski, E. Papis, K. Kosiel, M. Bugajski, M. Tlaczala, R. Jakiela, "Low resistance ohmic contacts to n-GaAs for application in GaAs/AlGaAs quantum cascade lasers," *Optica Applicata*, Vol. XXXXIX, No. 4, 2009

[47] L. Pauling, "The nature of the chemical bond. IV. The energy of single bonds and the relative electronegativity of atoms," Journal of the American Chemical Society, Vol. 54, pp. 3570-3582, 1932

[48] A.L. Allred and E. G. Rochow, "A Scale of Electronegativity Based on Electrostatic Force," *Journal of Inorganic and Nuclear Chemistry*, Vol. 5, pp. 264-268, 1958

[49] H.O. Pritchard, H.A. Skinner, "The Concept of Electronegativity," Chemical Reviews, Vol. 55, pp. 745-786, 1955

[50] F A Cotton, G Wilkinson, P L Gous, *Basic Inorganic Chemistry* (2nd edited), Wiley, 1987

[51] E H Rhoderick, R.H. Williams, *Metal–Semiconductor Contacts*, Plenum Press, 1984

[52] W Mönch, "On the physics of metal-semiconductor interfaces," *Report on Progress in Physics*, Vol. 53, pp. 221, 1990

[53] F D Auret, S.A. Goodman, G. Myburg and W.E. Meyer, "Electrical characterization of defects introduced in n-GaAs by alpha and beta irradiation from radionuclides," Applied Physics A, Vol. 56, pp. 547-553, 1993

[54] W. Macherzyński, M. Wośko, B. Paszkiewicz, B. Ściana, R. Paszkiewicz and M. Tłaczała, "Fabrication of ohmic contact based on platinum to p-type compositionally graded AlGaAs layers," *Journal of Physics: Conference Seriesi*, Vol. 146, 012034, 2009

[55] W. Shockley in A. Goetzberger and R. M. Scarlett. 1964 "Research and investigation of inverse Epitaxial UHF Power Transistors," Air Force Atomic Laboratory, Wright-Patterson AFB, Mak L K, Rogers C M, Northrop D C, 1989, *J. Phys. E: Sci. Instr.* 22 317

[56] H. A. Macleod, *Thin-Film Optical Filters* (3rd edited), London: Institute of Physics Publishing, 2001, pp. 23

[57] R.B. Pettit, C.J. Brinker, C.S. Ashley, “Sol–gel double-layer antireflection coatings for silicon solar cells,” *Solar Cells*, Vol. 15, pp. 267–278, 1985

[58] *http://refractiveindex.info*

[59] B.S. Richards, ”Single-material TiO_2 double-layer antireflection coatings,” *Solar Energy Materials and Solar Cells*, Vol. 79, pp. 369-390(22), Sep. 2003

[60] M.K. Song, W.S. Yang, S.W Kwon, Y-S Song, N. C. D.Y. Lee, “Influence of Deposition Method on Refractive Index of SiO2 and TiO2 Thin Films for Anti-reflective Multilayers,” *Journal of the Korean Ceramic Society*, Vol. 45, pp. 524-530, Jan. 2008

[61] K.N. Rao “Influnce of deposition parameters on optical properties of TiO2 films,” *Optical Engineering*, Vol. 41, pp. 2357-2364, Sep. 2002

[62] H.W. Lehmann, K. Frick, “Optimizing deposition parameters of electron beam evaporated TiO_2 films,” *Applied Optics*, Vol. 27, pp. 4920-4924, 1988

[63] P.P. Ewald, “Introduction to the dynamical theory of X-ray diffraction”, *Acta Crystallographica Section A*,Vol. 25, pp. 103, 1969

[64] R. A. Sinton and A. Cuevas, "A Quasi-Steady Open-Circuit Voltage Method for Solar Cell Characterization," *16th European PVSEC*, pp. 1152, 2000

[65] S. Bowden, V. Yelundur and A. Rohatgi, "Implied-V_{oc} and Suns-V_{oc} measurements in multicrystalline solar cells," *Photovoltaic Specialists Conference, 2002. Conference Record of the Twenty-Ninth IEEE* , vol. 371, no.374, pp. 19-24, May 2002

[66] D. K. Schroder, *Semiconductor material and device characterization (3rd edited)*, Hoboken, New Jersey: John Wiley & Sons, 2005, pp. 192-198